THE JOURNAL OF PHYSICAL CHEMISTRY C
Article
Cite This: J. Phys. Chem. C 2018, 122, 10343−10359
pubs.acs.org/JPCC

Combination of Charge Delocalization and Disorder Enables Efficient Charge Separation at Photoexcited Organic Bilayers

Veljko Janković and Nenad Vukmirović*

Scientific Computing Laboratory, Center for the Study of Complex Systems, Institute of Physics Belgrade, University of Belgrade, Pregrevica 118, Belgrade 11080, Serbia

Supporting Information

ABSTRACT: We study incoherent charge separation in a lattice model of an all-organic bilayer. Charge delocalization is taken into account by working in the basis of electron−hole pair eigenstates, and the separation is described as a series of incoherent hops between these states. We find that relatively weak energetic disorder, in combination with good charge delocalization, can account for efficient and weakly field- and temperature-dependent separation of the strongly bound charge transfer (CT) state. The separation efficiency is determined by the competition between the recombination from the initial CT state and the escape toward intermediate CT states, from which free-charge states can be reached with certainty. The separation of donor excitons also exhibits quite high yields, less bound excitons separating more efficiently. Overall, our results support the notion that efficient charge separation can be achieved even out of strongly bound pair states without invoking coherent effects.

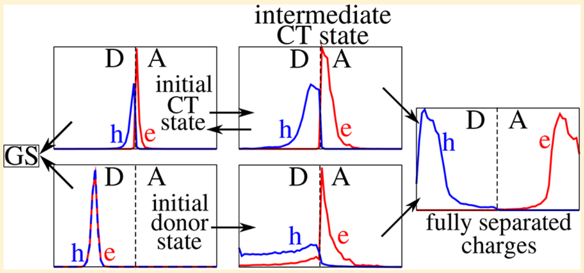

INTRODUCTION

The outstanding problem of charge carrier photogeneration at an interface between an electron-donating (donor) and an electron-accepting (acceptor) organic material has inspired coordinated and interdisciplinary research efforts in the field of organic photovoltaics (OPVs).[1−4] A photoexcitation of such an interface creates strongly bound donor (or acceptor) excitons that, after the diffusion to the donor/acceptor (D/A) interface, dissociate forming the charge transfer (CT) state. Although the magnitude of the Coulomb interaction between the electron and hole in the CT state is much larger than the thermal energy at room temperature, the subsequent charge separation and eventual formation of free charges that can be extracted at the electrodes is very efficient.[5,6]

Numerous mechanisms have been invoked to understand the origins of such an efficient conversion of strongly bound excitons to free charges. One group of mechanisms (coherent mechanisms) suggests that free-charge generation occurs on an ultrafast (100 fs) time scale by virtue of the high-energy ("hot") CT states in which electrons and holes are highly delocalized and spatially separated.[7−10] The charge separation competes with the subpicosecond exciton relaxation toward strongly bound and localized CT states, which are regarded as traps for further separation.[7] Another group of mechanisms (incoherent mechanisms) conceives charge separation as a much slower process that starts from the strongly bound ("cold") CT states and converts them into free carriers by means of the hopping between localized states that is possibly assisted by the interfacial electric field.[6,11−14] The characteristic time scale for the incoherent charge separation is of the order of tens to hundreds of picoseconds.[11,12] However, what actually drives the separation from "cold" CT states despite their strong binding and pronounced localization remains elusive.[2]

The coherent and incoherent separation mechanisms do not contradict each other, and both may be at play in an efficient OPV cell.[15] Indeed, from our recent theoretical studies,[16,17] which focus upon the ultrafast dynamics following photoexcitation of a model heterointerface, emerges that on picosecond time scales after photoexcitation the majority of charges are still bound in states of donor or CT excitons. In other words, there is some (coherent) charge separation on subpicosecond time scales, but the vast majority of charges remains in strongly bound states on picosecond time scales, which is in agreement with recent experimental results.[13] Therefore, examining charge separation on longer time scales is crucial to fully understand charge photogeneration in OPVs.

Recent theoretical studies have challenged the common view that the separation from the CT state requires surmounting an immense energy barrier.[18−21] These studies emphasize the influence of the entropy on charge separation. In this context, the entropy is related to the number of configurations in which an electron−hole pair may be arranged. It is suggested that the combined effect of entropy and disorder[20] or entropy and carrier delocalization[21] can substantially reduce (or even eliminate) the Coulomb barrier, so that the electron and hole in the CT state are not thermodynamically bound and thus might separate if there are no kinetic obstacles.

Received: April 2, 2018
Revised: April 19, 2018
Published: April 19, 2018

DOI: 10.1021/acs.jpcc.8b03114
J. Phys. Chem. C 2018, 122, 10343−10359

The charge separation from the strongly bound CT state has been extensively studied within the framework of the Onsager−Braun model[22,23] and its modifications.[24] Basically, the separation probability is determined by the competition between the electric field- and temperature-dependent dissociation of a localized electron−hole pair and its recombination to the ground state. While such a treatment has been revealed successful in reproducing experimental photodissociation yields in bulk molecular D/A crystals,[25] it has been recognized as unsuitable for conjugated polymer/fullerene blends.[26] The reasons for this inadequacy may be summarized as follows. First, the Onsager−Braun model employs the approximation of localized point charge carriers, which does not hold in a polymer/fullerene blend. In this regard, it has been proposed that the hole delocalization along conjugated segments of polymer chains can enhance charge separation[27−29] because the kinetic energy of hole oscillations along chains lowers the Coulomb barrier between the electron and hole. The combination of the effects due to the hole delocalization and the presence of dark interfacial dipoles[30,31] has been demonstrated to reproduce the essential features of experimental photocurrent data.[32] Furthermore, the combination of the on-chain hole delocalization and the dimensional (entropic) effects has been suggested as the main reason for weakly field-dependent and very efficient charge separation in polymer/fullerene bilayers.[33] Second, for the Onsager−Braun model to reproduce experimental data, the mobility-lifetime product should assume unrealistically high values, meaning that either carrier mobility or pair lifetime should be unrealistically large. Kinetic Monte Carlo (kMC) studies have demonstrated that efficient and weakly field- and temperature-dependent charge separation can be achieved when relevant parameters are carefully chosen on the basis of experimental data.[34,35] Third, the Onsager−Braun model does not capture the effects of the (energetic and/or spatial) disorder on charge separation. In ref 36, an analytical treatment of charge separation in a one-dimensional disordered chain is presented, and it was suggested that, at least at low interfacial electric fields, the disorder may enhance the separation of geminate electron−hole pairs. Recent kMC results also point toward the beneficial role of not too strong energetic disorder on charge separation.[37]

Here, we investigate the separation of geminate electron−hole pairs in a one-dimensional lattice model of a bilayer. The model takes into account energetic disorder, carrier delocalization, carrier−carrier interaction, carrier recombination, and the interaction of carriers with the phonon bath and the interfacial electric field. The carrier delocalization is properly taken into account by transferring the description of charge separation from the usually used position space to the space spanned by the exciton basis states, that is, by stationary states of an electron−hole pair on the model interface. The charge separation is then concieved as a sequence of transitions between exciton basis states that are mediated by the interaction with the phonon bath. The separation yield is computed from the stationary solution to the rate equations for basis states populations in two cases, for the separation starting from CT states and donor exciton states. We find that moderate energetic disorder and carrier delocalization promote efficient and relatively weakly field-dependent separation of the strongly bound CT exciton. In this process, the vital role is played by long-lived intermediate CT states, from which further charge separation proceeds practically without obstacles. The separation of the strongly bound donor exciton is also efficient, but requires quite strong electric fields to occur with certainty. On the other hand, more separated and weakly bound donor excitons separate with efficiency close to 1.

MODEL AND METHODS

Model Hamiltonian, Exciton States, and Their Classification. To describe the bilayer of two organic semiconductors, we employ the standard semiconductor model on a lattice with multiple single-electron and single-hole states per site. The model to be presented is quite general and may also be used (upon appropriate adjustments) to study the electric field-assisted charge generation in other D/A structures. The numerical computations are performed on a one-dimensional system consisting of $2N$ sites located on a lattice of constant a. The sites $0,...,N-1$ represent the donor part, while sites $N,...,2N-1$ represent the acceptor part of the bilayer. The single-electron levels on lattice site i are counted by index β_i, so that Fermi operators $c^\dagger_{i\beta_i}$ ($c_{i\beta_i}$) create (destroy) an electron on site i and in single-electron state β_i. The single-hole levels on site i are counted by index α_i, and Fermi operators $d^\dagger_{i\alpha_i}$ ($d_{i\alpha_i}$) create (annihilate) a hole in single-hole state α_i on site i. The phonon bath is assumed to consist of a multitude of localized phonon modes on each lattice site, and the sets of phonon modes on all sites are identical. The Bose operators $b^\dagger_{i\lambda}$ ($b_{i\lambda}$) create (annihilate) a phonon on site i and in phonon mode λ. The model Hamiltonian assumes the form:

$$H = H_\mathrm{c} + H_\mathrm{p} + H_\mathrm{c-p} + H_\mathrm{c-f} \tag{1}$$

where H_c describes interacting carriers:

$$\begin{aligned} H_\mathrm{c} = {} & \sum_{\substack{i\beta_i \\ j\beta'_j}} \varepsilon^\mathrm{c}_{(i\beta_i)(j\beta'_j)} c^\dagger_{i\beta_i} c_{j\beta'_j} - \sum_{\substack{i\alpha_i \\ j\alpha'_j}} \varepsilon^\mathrm{v}_{(i\alpha_i)(j\alpha'_j)} d^\dagger_{i\alpha_i} d_{j\alpha'_j} \\ & + \frac{1}{2} \sum_{\substack{i\beta_i \\ j\beta'_j}} V_{ij} c^\dagger_{i\beta_i} c^\dagger_{j\beta'_j} c_{j\beta'_j} c_{i\beta_i} + \frac{1}{2} \sum_{\substack{i\alpha_i \\ j\alpha'_j}} V_{ij} d^\dagger_{i\alpha_i} d^\dagger_{j\alpha'_j} d_{j\alpha'_j} d_{i\alpha_i} \\ & - \sum_{\substack{i\beta_i \\ j\alpha_j}} V_{ij} c^\dagger_{i\beta_i} d^\dagger_{j\alpha_j} d_{j\alpha_j} c_{i\beta_i} \end{aligned} \tag{2}$$

$$H_\mathrm{p} = \sum_{i\lambda} \hbar\omega_\lambda b^\dagger_{i\lambda} b_{i\lambda} \tag{3}$$

describes the phonon bath, $H_\mathrm{c-p}$ accounts for the interaction of carriers with the phonon bath:

$$\begin{aligned} H_\mathrm{c-p} = {} & \sum_{i\beta_i} \sum_{\lambda} g^\mathrm{c}_{i\beta_i\lambda} c^\dagger_{i\beta_i} c_{i\beta_i} (b^\dagger_{i\lambda} + b_{i\lambda}) \\ & - \sum_{i\alpha_i} \sum_{\lambda} g^\mathrm{v}_{i\alpha_i\lambda} d^\dagger_{i\alpha_i} d_{i\alpha_i} (b^\dagger_{i\lambda} + b_{i\lambda}) \end{aligned} \tag{4}$$

whereas $H_\mathrm{c-f}$ represents the interaction of carriers with the interfacial electric field $\mathbf{F}$, which is assumed to be uniform throughout the system:

$$H_\mathrm{c-f} = \sum_{i\beta_i} q\mathbf{F}\cdot\mathbf{r}_i\, c^\dagger_{i\beta_i} c_{i\beta_i} - \sum_{i\alpha_i} q\mathbf{F}\cdot\mathbf{r}_i\, d^\dagger_{i\alpha_i} d_{i\alpha_i} \tag{5}$$

In eq 2, we take that quantities $\varepsilon^\mathrm{c}_{(i\beta_i)(j\beta'_j)}$ ($\varepsilon^\mathrm{v}_{(i\alpha_i)(j\alpha'_j)}$), which represent electron (hole) on-site energies and transfer integrals, assume nonzero values only for particular combinations of their indices. In more detail, we assume that $\varepsilon^{\mathrm{c}}_{(i\beta_i)(j\beta'_j)} \neq 0$ when it represents

(1) on-site energy $\varepsilon^{\mathrm{c}}_{i\beta_i}$ of single-electron level β_i on site i, for $i = j$ and $\beta_i = \beta'_i$;

(2) negative electron transfer integral between single-electron levels on nearest-neighboring sites belonging to the same band β_i, $-J^{\mathrm{c,int}}_{i\beta_i}$, for i and j both belonging to the same part of the bilayer, $|i - j| = 1$, and $\beta_i = \beta'_j$;

(3) negative electron transfer integral between single-electron levels on nearest-neighboring sites belonging to different bands, $-J^{\mathrm{c,ext}}_{i\beta_i\beta'_j}$, for i and j both belonging to the same part of the bilayer, $|i - j| = 1$, and $\beta_i \neq \beta'_j$; or

(4) negative electron transfer integral between different parts of the bilayer, $-J^{\mathrm{c}}_{\mathrm{DA}}$, for $i = N - 1$ and $j = N$ or vice versa.

The Coulomb interaction (eq 2) is taken into account in the lowest monopole−monopole approximation, and the interaction potential V_{ij} is assumed to be the Ohno potential:

$$V_{ij} = \frac{U}{\sqrt{1 + \left(\frac{r_{ij}}{r_0}\right)^2}} \tag{6}$$

where U is the on-site Coulomb interaction, r_{ij} is the distance between sites i and j, $r_0 = q^2/(4\pi\varepsilon_0\varepsilon_{\mathrm{r}}U)$ is the characteristic length, and ε_{r} is the relative dielectric constant. Charge carriers are assumed to be locally and linearly coupled to the phonon bath (Holstein-type interaction), as given in eq 4. In eq 5, $q > 0$ is the elementary charge, $\mathbf{r}_i$ is the position vector of site i, and vector $\mathbf{F}$ is assumed to be perpendicular to the interface and directed opposite the internal electric field of a space-separated electron−hole pair (vide infra). The interfacial electric field may originate from the different Fermi levels of the electrodes,[38] or from some other source.[39]

Similar to other numerical studies, which obtain charge separation efficiency by tracking the faith of a single electron−hole pair, we confine ourselves to the subspace of a single electron−hole pair. We describe charge separation in the exciton basis, whose basis vectors are stationary states of an electron−hole pair supported by the model interface. The most general state of an electron−hole pair can be written as $|x\rangle = \sum_{\substack{i\alpha_i \\ j\beta_j}} \psi^x_{(i\alpha_i)(j\beta_j)} c^\dagger_{j\beta_j} d^\dagger_{i\alpha_i} |0\rangle$, where $|0\rangle$ is the vacuum of electron−hole pairs. The exciton basis states are obtained by solving the eigenvalue problem $(H_{\mathrm{c}} + H_{\mathrm{c-f}})|x\rangle = \hbar\omega_x|x\rangle$, which in the basis of single-particle states localized at lattice sites reads as

$$\sum_{\substack{i'\alpha'_i \\ j'\beta'_j}} \Big(\delta_{ii'}\delta_{\alpha_i\alpha'_i}\varepsilon^{\mathrm{c}}_{(j\beta_j)(j'\beta'_j)} - \delta_{jj'}\delta_{\beta_j\beta'_j}\varepsilon^{\mathrm{v}}_{(i\alpha_i)(i'\alpha'_i)} - \delta_{ii'}\delta_{\alpha_i\alpha'_i}\delta_{jj'}\delta_{\beta_j\beta'_j} \times (V_{ij} - q\mathbf{F}\cdot(\mathbf{r}_j - \mathbf{r}_i))\Big)\psi^x_{(i'\alpha'_i)(j'\beta'_j)} = \hbar\omega_x\psi^x_{(i\alpha_i)(j\beta_j)} \tag{7}$$

We take into account the diagonal static disorder; that is, on-site energies $\varepsilon^{\mathrm{c}}_{i\beta_i}$ and $\varepsilon^{\mathrm{v}}_{i\alpha_i}$ depend on site index i. The disorder is the essential element of our model, because disorder-induced localization effects enable us to isolate exciton states that are similar to states of free charges, as will be detailed in the next paragraph.

It is convenient to classify the exciton basis states in a manner similar to that we employed in our previous studies,[16,17] where we differentiated between

(1) donor exciton (XD) states, in which both carriers are mainly in the donor part of the bilayer,

(2) acceptor exciton (XA) states, in which both carriers are mainly in the acceptor part of the bilayer, and

(3) space-separated exciton states, in which the electron is mainly in the acceptor, while the hole is mainly in the donor part of the bilayer.

Here, we are interested in full charge separation, which results in almost free carriers capable of producing electric current. Therefore, we have to individuate exciton states of our model that resemble these free-carrier states. To this end, we introduce the notion of the contact region of the bilayer, which consists of sites $0,\ldots,l_{\mathrm{c}} - 1$ in the donor part and sites $2N - l_{\mathrm{c}},\ldots,2N - 1$ in the acceptor part of the bilayer. If both electron and hole are primarily located in the contact region (the electron in its acceptor part and the hole in its donor part), we consider them as fully separated carriers. More quantitatively, we say that space-separated exciton state x is a contact state (state of fully separated carriers) if

$$\sum_{i=0}^{l_{\mathrm{c}}-1} \sum_{j} \sum_{\alpha\beta_j} |\psi^x_{(i\alpha_i)(j\beta_j)}|^2 \geq 0.7 \tag{8}$$

and

$$\sum_{i} \sum_{j=2N-l_{\mathrm{c}}}^{2N-1} \sum_{\alpha\beta_j} |\psi^x_{(i\alpha_i)(j\beta_j)}|^2 \geq 0.7 \tag{9}$$

The space-separated states that are not contact states will be further referred to as CT states. We point out that the localization induced by disorder is crucial to identify contact states. In the perfectly ordered system, there are no space-separated states that meet the criteria of spatial localization given in eqs 8 and 9.

Theoretical Approach to Incoherent Charge Separation. Our aim is to analyze the incoherent charge separation, that is, charge separation that occurs on long time scales so that coherent features are not pronounced and consequently carrier dynamics can be well described in terms of populations only. Here, we work in the basis of electron−hole pair states x and study charge separation by finding a stationary solution to an appropriate equation for populations f_x of exciton states. Similar to ref 36, we assume that contact states act as absorbing states in the course of charge separation; that is, once an exciton reaches a contact state, it is removed from the system. This removal may be interpreted as the extraction of the fully separated electron and hole at the electrodes. Therefore, we find the stationary solution to equations for populations f_x of exciton states x that do not belong to the group of contact states (further denoted as C). These equations are Pauli master equations in which the interaction with the phonon bath leads to transitions between exciton states. The time evolution of the population of exciton state $x \notin C$ is described by

$$\frac{\mathrm{d}f_x}{\mathrm{d}t} = g_x - \tau_x^{-1} f_x - \sum_{x'} w_{x'x} f_x + \sum_{x' \notin C} w_{xx'} f_{x'} \tag{10}$$

where g_x is the generation rate of state x (the number of excitons generated per unit time in state x), τ_x is the lifetime of exciton state x, $w_{x'x}$ is the rate of phonon bath-induced transition from state x to state x', while the condition $x' \notin C$ on the summation in the fourth term is due to the assumption of absorbing contact states.

We searching for the stationary solution f_x^0 to eq 10, which satisfies

$$0 = g_x - \tau_x^{-1} f_x^0 - \sum_{x'} w_{x'x} f_x^0 + \sum_{x' \notin C} w_{xx'} f_{x'}^0 \tag{11}$$

With the stationary populations of exciton states at hand, we can compute the separation probability:

$$\varphi = \frac{\sum_{x' \in C} \sum_{x \notin C} w_{x'x} f_x^0}{\sum_{x \notin C} g_x} \tag{12}$$

and the recombination probability:

$$\rho = \frac{\sum_{x \notin C} \tau_x^{-1} f_x^0}{\sum_{x \notin C} g_x} \tag{13}$$

Using eq 10, it can be shown that $\varphi + \rho = 1$. Different choices of g_x allow us to investigate incoherent charge separation starting from different initial states.

The phonon bath-assisted transition rates from exciton state x to exction state x', $w_{x'x}$, can be obtained using the Fermi golden rule. First, it is convenient to rewrite the carrier–phonon bath interaction $H_{\text{c-p}}$ (eq 4) in the relevant subspace of single electron–hole excitations as[16]

$$H_{\text{c-p}} = \sum_{\substack{x'x \\ i\lambda}} \Gamma_{x'x}^{i\lambda} |x'\rangle\langle x| (b_{i\lambda}^\dagger + b_{i\lambda}) \tag{14}$$

where the interaction constants in the exciton basis read as

$$\Gamma_{x'x}^{i\lambda} = \sum_{\beta_i} \sum_{j\alpha_j} g_{i\beta_i\lambda}^{\text{c}} \psi_{(j\alpha_j)(i\beta_i)}^{x'*} \psi_{(j\alpha_j)(i\beta_i)}^{x} - \sum_{\alpha_i} \sum_{j\beta_j} g_{i\alpha_i\lambda}^{\text{v}} \psi_{(i\alpha_i)(j\beta_j)}^{x'*} \psi_{(i\alpha_i)(j\beta_j)}^{x} \tag{15}$$

Therefore, the phonon bath-assisted transition rate from state x to state x' is

$$w_{x'x} = \frac{2\pi}{\hbar} \sum_{i\lambda} |\Gamma_{x'x}^{i\lambda}|^2 \delta(\hbar\omega_{x'} - \hbar\omega_x - \hbar\omega_\lambda) n_{\text{BE}}(\hbar\omega_\lambda) + \frac{2\pi}{\hbar} \sum_{i\lambda} |\Gamma_{x'x}^{i\lambda}|^2 \delta(\hbar\omega_{x'} - \hbar\omega_x + \hbar\omega_\lambda)(1 + n_{\text{BE}}(\hbar\omega_\lambda)) \tag{16}$$

where $n_{\text{BE}}(E) = (e^{\beta E} - 1)^{-1}$ is the Bose–Einstein occupation number at temperature $T = (k_B\beta)^{-1}$. The right-hand side of eq 16 can be simplified by assuming that all of the interaction constants $g_{i\beta\lambda}^{\text{c}}$ and $g_{i\alpha\lambda}^{\text{v}}$ are independent of site and band indices and equal to g_λ. Introducing the spectral density $J(E)$ by

$$J(E) = \sum_\lambda |g_\lambda|^2 \delta(E - \hbar\omega_\lambda) \tag{17}$$

we obtain

$$w_{x'x} = \frac{2\pi}{\hbar} P_{x'x} J(|\hbar\omega_{x'} - \hbar\omega_x|) n(\hbar\omega_{x'} - \hbar\omega_x) \tag{18}$$

where

$$P_{x'x} = \sum_i \left| \sum_{\beta_i} \sum_{j\alpha_j} \psi_{(j\alpha_j)(i\beta_i)}^{x'*} \psi_{(j\alpha_j)(i\beta_i)}^{x} - \sum_{\alpha_i} \sum_{j\beta_j} \psi_{(i\alpha_i)(j\beta_j)}^{x'*} \psi_{(i\alpha_i)(j\beta_j)}^{x} \right|^2 \tag{19}$$

whereas

$$n(E) = \begin{cases} n_{\text{BE}}(E), & E > 0 \\ 1 + n_{\text{BE}}(-E), & E < 0 \end{cases} \tag{20}$$

The transition rates $w_{x'x}$ do not depend solely on the energy difference $\hbar\omega_{x'} - \hbar\omega_x$ between exciton states x' and x, but also on spatial properties (e.g., spatial localization and mutual overlap) of these states, which is described by quantity $P_{x'x}$ (the so-called spatial proximity factor). The spatial proximity factor between exciton states of the same character is in general much larger than that between states of different characters. In other words, for the same energy difference $\hbar\omega_{x'} - \hbar\omega_x$, the transition probability $w_{x'x}$ (eq 18) is much larger when states x' and x are of the same character than when their characters are different. The last point will be repeatedly used in further discussion.

Parametrization of the Model Hamiltonian. The values of model parameters used in our computations are summarized in Table 1. They are selected so that the values of band gaps, bandwidths, band offsets, and binding energies of the donor, acceptor, and CT exciton that emerge from our model are in agreement with the literature values for typical OPV materials. While the present values are largely chosen to be representative of the P3HT/PCBM interface, we emphasize that our aim is to unveil fundamental physical effects responsible for very efficient charge separation at an all-organic bilayer. Therefore, many of the parameters listed in Table 1 will be varied (within reasonable limits), and the effects of these variations on charge

Table 1. Values of Model Parameters Used in Computations

parameter	value
N	30
l_c	11
a (nm)	1.0
U (eV)	0.65
ε_r	3.0
$\varepsilon_{D,0}^{c}$ (eV)	2.63
$J_{D,0}^{c,int}$ (eV)	0.1
$\varepsilon_{D,0}^{v}$ (eV)	−0.3
$J_{D,0}^{v,int}$ (eV)	−0.15
$\varepsilon_{A,0}^{c}$ (eV)	1.565
$\varepsilon_{A,1}^{c}$ (eV)	1.865
$J_{A,0}^{c,int}$ (eV)	0.05
$J_{A,1}^{c,int}$ (eV)	0.025
$J_{A,01}^{c,ext}$ (eV)	0.02
$\varepsilon_{A,0}^{v}$ (eV)	−1.03
$J_{A,0}^{v,int}$ (eV)	−0.15
J_{DA}^{c} (eV)	0.1
J_{DA}^{v} (eV)	−0.1
σ (meV)	50
η	1.5
E_c (meV)	10
τ_0 (ps)	250
$A_{A/D}$	0.5
T (K)	300

separation yield will be rationalized. This is also of practical relevance, because the trends observed in such variations may suggest which material properties should be tuned to maximize the separation efficiency.

Actual computations are performed on the model system having one single-electron level per site in the donor and one single-hole level per site in both the donor and the acceptor. To mimic the presence of higher-than-LUMO orbitals energetically close to the LUMO level, which is a situation typical of fullerenes,[40,41] we take two single-electron levels per acceptor site. The HOMO level of the ordered donor material is taken as the zero of the energy scale. The model is schematically depicted in Figure 1. The choice of the values of model parameters is almost the same as in our recent investigation of ultrafast dynamics at a D/A heterointerface.[16] Therefore, here, we only briefly summarize the essential features of this parameter set, while the details can be found in our recent article.

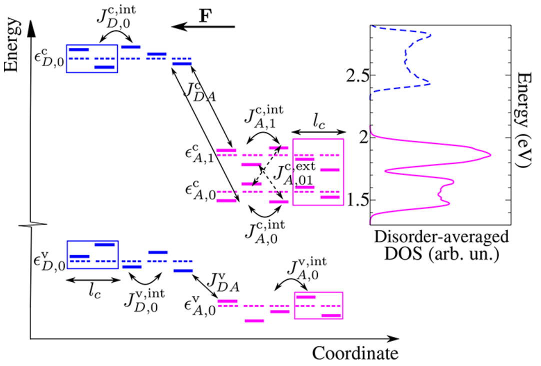

Figure 1. Schematic view of the model system indicating different transfer integrals and average on-site energies listed in Table 1. The dashed lines represent average on-site energies, while the solid lines represent actual on-site energies, which vary from site to site due to the diagonal static disorder. The contact region of the bilayer is denoted by rectangles. **F** is the vector of the interfacial electric field. The plot on the right presents the single-particle DOS for electrons in the isolated acceptor (full line) and donor (dashed line) regions of the bilayer averaged over different disorder realizations. For each disorder realization, the electronic states of the isolated regions are obtained by diagonalizing the free-electron Hamiltonian (the first term on the right-hand side of eq 2) in which the D/A coupling J^{c}_{DA} is set to 0. The DOS for that disorder realization is computed by broadening each of the single-electron states obtained by a Gaussian whose standard deviation is equal to 10 meV.

Within each region of the bilayer, the on-site energies of electrons and holes are drawn from a Gaussian distribution function. For example, the probability density that the energy of the electron on donor site i $(0 \le i \le N - 1)$ is in the vicinity of $\varepsilon^{c}_{i,0}$ can be expressed as

$$f(\varepsilon^{c}_{i,0}) = \frac{1}{\sigma\sqrt{2\pi}} \exp\left(-\frac{(\varepsilon^{c}_{i,0} - \varepsilon^{c}_{D,0})^2}{2\sigma^2}\right) \tag{21}$$

where $\varepsilon^{c}_{D,0}$ is the average electron on-site energy in the donor, and σ is the standard deviation of the Gaussian distribution. We assume that the deviations of on-site energies from their average values are uncorrelated; this assumption regards both on-site energies of electrons (holes) on different sites and on-site energies of electrons and holes on the same site. The disorder strength is determined by parameter σ, which typically assumes values of the order of 100 meV.[42] To obtain analytical insights into charge separation efficiency, we opt for a lower value of $\sigma = 50$ meV, which does lead to localization effects, but does not completely destroy charge delocalization. Moreover, the disorder-averaged values of relevant quantities, such as exciton binding energies, LUMO−LUMO, and HOMO−HOMO offsets, assume values that are quite close (within few tens of meV) to the respective values in the ordered system, which will thus often be used in the discussion.

The lattice constant a is comparable to typical distances between neighboring constitutive elements of ordered polymers[43] (fullerene aggregates[44]). The number N of lattice sites in the donor and acceptor is then chosen so that the length of the model bilayer is similar to the linear dimensions of the polymer/fullerene bilayers used in experiments.[26,29,32] Our choice of the value of the hole transfer integral $J^{v,int}_{D,0}$ is motivated by the literature values of the HOMO bandwidth along the π-stacking direction of the regioregular P3HT[45,46] and the values of the hole transfer integral along the π-stacking direction of the same material.[47,48] Such a choice tacitly assumes that the hole transport in the donor part of the bilayer takes place among different polymer chains. However, our Hamiltonian is quite general, so that a different selection of the values of its parameters can describe a different physical situation, for example, the hole transport along a polymer chain. The single-particle and optical gap of the ordered donor part of the bilayer are tuned to be around 2.43 and 2.0 eV, respectively,[49,50] so that the exciton binding energy of the ordered donor material is around 0.43 eV. The electronic parameters of the acceptor (transfer integrals $J^{c,int}_{A,0}$, $J^{c,int}_{A,1}$, and $J^{c,ext}_{A,01}$ and the energy difference $\varepsilon^{c}_{A,1} - \varepsilon^{c}_{A,0}$ between average values of electronic on-site energies) are selected so that the single-electron density of states (DOS) of the ordered acceptor part reproduces the most important features of the DOS of fullerene aggregates.[40,51] The single-particle gap and the binding energy of the ordered acceptor part are tuned to the values of around 2.2 and 0.45 eV.[49] The values of the LUMO−LUMO (ca. 0.97 eV) and HOMO−HOMO (ca. 0.73 eV) offsets between the donor and acceptor part of the ordered bilayer are chosen by adjusting the energy differences Δ_{XD-CT} and Δ_{XA-CT} between the lowest excited state of the heterojunction (the lowest CT state) and the lowest exciton states in the donor and acceptor to the typical literature values.[49,52,53] The magnitudes of the transfer integrals J^{c}_{DA} and J^{v}_{DA} between the two materials are taken to be similar to the values obtained in ref 54.

For the spectral density of the phonon bath, we take the Ohmic spectral density:[55]

$$J(E) = \eta E \, e^{-E/E_c} \tag{22}$$

which is characterized by two parameters: the dimensionless parameter η describes the strength of the system−bath coupling, while E_c is the energy cutoff determining the energy range of phonon modes that are strongly coupled to the system. For the Holstein-like system−bath coupling and in the limiting case of a charge carrier localized on a single lattice site, the polaron binding energy is given by $E_{pol} = \sum_\lambda |g_\lambda|^2/(\hbar\omega_\lambda)$.[56] In terms of spectral density $J(E)$, and specifically for the Ohmic spectral density, the polaron binding energy can be expressed as

$$E_{pol} = \int_0^{+\infty} dE \frac{J(E)}{E} = \eta E_c \tag{23}$$

DOI: 10.1021/acs.jpcc.8b03114
J. Phys. Chem. C 2018, 122, 10343−10359

It is equal to the geometry relaxation energy Λ_{rel} upon charging a molecule and to one-half of the reorganization energy Λ_{reorg}.[56] In ref 40, the relaxation energy of the $PC_{60}BM$ anion was estimated to be $\Lambda_{rel} = 15$ meV. The authors of ref 57 found that the polaron binding energy in a long straight polythiophene chain is of the order of 10 meV. We use these estimates and take the polaron binding energy $E_{pol} = 15$ meV (the reorganization energy is then $\Lambda_{reorg} = 30$ meV). We assume that the system–bath coupling is strongest for the low-frequency phonon modes and therefore take that $E_c = 10$ meV and $\eta = 1.5$. All of these assumptions will be reassessed in the Discussion.

There are different kinds of recombination processes that limit the efficiency of organic solar cells.[58] The recombination of an electron–hole pair that originates from the absorption of a single photon is geminate recombination. On the other hand, an electron and a hole undergoing a nongeminate recombination event do not originate from the same photon. Here, we consider only geminate recombination, which at a D/A interface may occur as (a) the recombination of excitons photogenerated in a neat donor or acceptor material, or (b) the recombination of excitons in CT states. The recombination can be further classified as radiative or nonradiative. In neat polymers, recombination predominantly occurs via nonradiative processes.[59] In D/A blends, the major part of charges recombine nonradiatively either at the interface or in the donor material.[60] However, there is no simple model that describes the rate of nonradiative recombination in terms of microscopic material properties. It is intuitively clear that the smaller is the overlap between the electron and hole probability densities, the smaller is the rate of their recombination and the larger is the lifetime of the pair. In previous model studies of charge separation at D/A interfaces, the last point has been recognized as the steep dependence of the exciton lifetime on the electron–hole separation,[61] so that the recombination is assumed to occur exclusively from the strongly bound CT state,[32,36,61] or a formula describing the aforementioned distance dependence is proposed.[33] Here, to each exciton state x, be it a state in the neat material or a CT state, we assign the lifetime τ_x that is inversely proportional to the weighted overlap of the electron and hole wave function moduli:

$$\tau_x = \tau_0 \left(\sum_{i=0}^{N-1} |\phi_i^{x,\mathrm{e}}||\phi_i^{x,\mathrm{h}}| + A_{\mathrm{A/D}} \sum_{i=N}^{2N-1} |\phi_i^{x,\mathrm{e}}||\phi_i^{x,\mathrm{h}}| \right)^{-1} \tag{24}$$

In the last expression, the moduli of the wave function of the electron and hole in exciton state x are defined as

$$|\phi_i^{x,\mathrm{e}}| = \sqrt{\sum_{\beta_i} \sum_{j\alpha_j} |\psi^x_{(j\alpha_j)(i\beta_i)}|^2} \tag{25}$$

$$|\phi_i^{x,\mathrm{h}}| = \sqrt{\sum_{\alpha_i} \sum_{j\beta_j} |\psi^x_{(i\alpha_i)(j\beta_j)}|^2} \tag{26}$$

while τ_0 and $A_{A/D}$ are constants that are determined so that the lifetimes of the lowest CT, XD, and XA states in the ordered system agree with the values reported in the literature. The expression for the lifetime given in eq 24 captures the previously described trend. Singlet exciton lifetimes in a variety of conjugated polymers used in organic solar cells are of the order of hundreds of picoseconds.[59] Time-resolved photoluminescence measurements yield the singlet exciton lifetime in neat P3HT around 470 ps and in neat PCBM around 740 ps.[62] From the transient absorption measurements performed in blends of P3HT and different fullerenes, the lifetime of the CT state was determined to be around 3 ns.[63] For the values of model parameters listed in Table 1, the lifetime of the lowest CT state in the ordered system is $\tau_{CT}^{ord} \approx 2.5$ ns, the lifetime of the lowest XD state in the ordered system is $\tau_{XD}^{ord} \approx 400$ ps, and the lifetime of the lowest XA state in the ordered system is $\tau_{XA}^{ord} \approx 800$ ps.

■ NUMERICAL RESULTS

In this section, we present the results concerning the yield of charge separation starting from CT and donor states. In all of the computations, we average over different disorder realizations, and all of the results to be presented are averaged over 256 disorder realizations. To facilitate the discussion, in Figure 2a–e we present disorder-averaged DOS for different groups of exciton states. Similar to our recent study, we discriminate between CT states belonging to CT_0 and CT_1 bands.[16] We say that a CT state belongs to the CT_0 (CT_1) band if its electron primarily belongs to the electronic band in the acceptor part of the bilayer arising from the single-electron level of average energy $\varepsilon^c_{A,0}$ ($\varepsilon^c_{A,1}$).

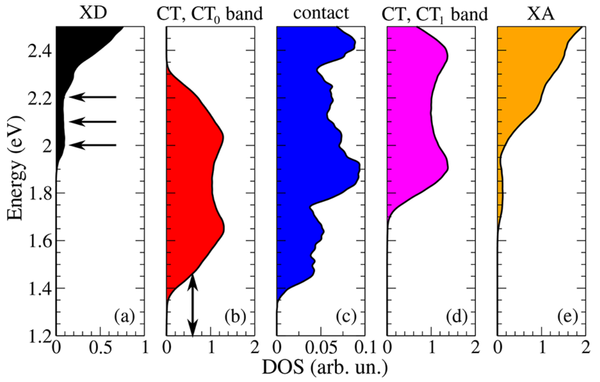

Figure 2. Disorder-averaged exciton DOS (in arbitrary units and at $F = 0$) for (a) donor exciton states, (b) CT states belonging to CT_0 band, (c) contact states, (d) CT states belonging to CT_1 band, and (e) acceptor exciton states. The horizontal arrows in (a) indicate approximate energies of XD states serving as initial states of charge separation. The vertical double-sided arrow in (b) indicates the energy range of the CT states acting as initial states of charge separation. The DOS in a single disorder realization is obtained by broadening each exciton level by a Gaussian whose standard deviation is equal to 10 meV.

Charge Separation from the Strongly Bound CT State. As starting states for the charge separation process, here we consider CT states belonging to the CT_0 band. One particular CT state out of all of the states in the CT_0 band is chosen by requiring that the mean electron–hole separation, which for exciton state x reads as

$$\langle r_{\mathrm{e-h}} \rangle_x = \sum_{\substack{i\alpha_i \\ j\beta_j}} |i-j||\psi^x_{(i\alpha_i)(j\beta_j)}|^2 \tag{27}$$

be minimal. We will further refer to such a state as the strongly bound CT state. The strongly bound CT state is located on the lower edge of the disorder-averaged DOS of CT excitons belonging to the CT_0 band; see the vertical double-sided arrow in Figure 2b. We set the generation rate g_x appearing in eq 10 to be different from zero only for the strongly bound CT state.

The field-dependent separation yield from this state is presented by circles in Figure 3a. The separation yield is above 0.6 for all of the examined values of the electric field down to $F = 0$. Figure 3b presents the low-energy tail of the DOS of contact states (see Figure 2c) along with the distribution of energies of the lowest-energy contact state. Figure 3c shows the low-energy tail of the DOS of CT states (see Figure 2b) together with the distribution of energies of the initial strongly bound CT state. The disorder-averaged energy difference between the lowest-energy contact state and the initial CT state may serve as an estimate of the average energy barrier that an electron–hole pair in the initial CT state has to surmount to reach the nearest free-charge state. We obtain the average barrier of approximately 0.13 eV ($\sim 5\ k_B T$ at room temperature), which is lower (at least by a factor of 2) than usually assumed when considering separation of the strongly bound CT exciton.[64] Further discussion reveals that the actual barrier to be overcome is smaller than the energy difference between the lowest-energy contact state and the initial CT state. The intermediate CT states, lying between the initial CT state and the lowest-energy contact state and exhibiting larger electron–hole distances as compared to the initial CT state, are crucial to the successful separation of the initial strongly bound pairs. Stronger electric field is beneficial to exciton separation, which, combined with the fact that the separation yield is above 0.5 even at $F = 0$, implies that it exhibits relatively weak dependence on the magnitude of the electric field.

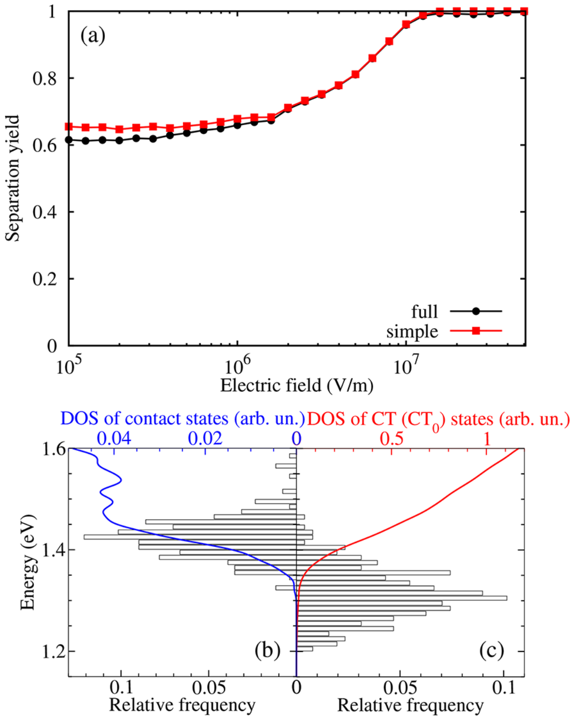

Figure 3. (a) Field-dependent yield of charge separation from the strongly bound CT state. The data labeled by "full" are obtained by numerically solving eq 10, while the data labeled by "simple" are computed using eq 34. The low-energy edges of the disorder-averaged DOS (full lines) for (b) contact states and (c) CT states belonging to the CT_0 band. The bars depict histograms of the distribution of the energy of (b) the lowest-energy contact state and (c) the initial strongly bound CT state. The width of the bins on the energy axis is 10 meV, while $F = 0$.

It is instructive to analyze the results presented in Figure 3a from the viewpoint of single disorder realizations. In Figure 4a–d we present distributions of the separation yield in single disorder realizations at different strengths of the electric field. A distinctive feature of all of the histograms is a quite small number of disorder realizations for which the separation yield assumes values in an intermediate range (say between 0.2 and 0.8). Even at zero electric field, the number of disorder realizations in which the separation yield is high (above 0.8) is greater than the number of those in which the separation yield is low (below 0.2), which can account for the mean separation yield above 0.5 even at zero field. As the electric field is increased, the number of disorder realizations in which the separation yield is low or intermediate decreases, while the number of disorder realizations in which the separation yield is high increases; see Figure 4b–d. At $F = 10^7$ V/m, the separation yield is between 0.95 and 1 for somewhat less than 90% of disorder realizations, see Figure 4d, meaning that the mean yield is close to 1. Relevant to this discussion are also the relative positions of the lower-energy tails of the DOS of CT states belonging to the CT_0 band and the DOS of contact states, which are presented in Figure S1a–d. We observe that the effect of increasing F on the DOS tails consists of decreasing the energy difference between the edges of CT and contact DOS. For sufficiently strong field, the lowest contact state is situated energetically below the strongly bound CT state.

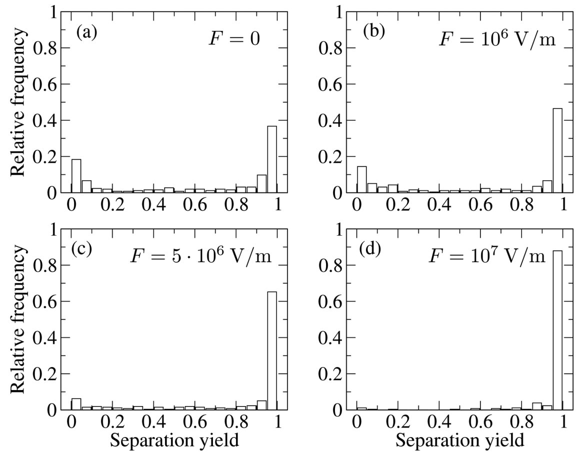

Figure 4. Histograms showing the distribution of the yield of charge separation from the strongly bound CT state for different strengths of the electric field: (a) $F = 0$, (b) $F = 10^6$ V/m, (c) $F = 5 \times 10^6$ V/m, and (d) $F = 10^7$ V/m. The width of the bins for the separation yield is 0.05.

We now establish which factors primarily determine the separation yield and propose an analytical formula that is capable of reproducing the separation yield in single disorder realizations (and consequently the mean separation yield) quite well. Let us begin by noticing that the initial CT state is usually strongly coupled (by means of phonon bath-assisted transitions) to only a couple of exciton states, which are of CT character and whose electron–hole separation (and consequently the lifetime) is larger than in the initial CT state. We further refer to these states as intermediate states. Moreover, intermediate states are in general very well coupled to other space-separated states, meaning that, in principle, there is no kinetic obstacle for an exciton in the intermediate state to undergo a series of phonon bath-assisted transitions in which the electron−hole separation gradually increases, and finally reach a contact state. However, because the coupling among the initial state and intermediate states is appreciable, the “implosion” of the pair, that is, the back-transfer from intermediate states to the initial CT state followed by the recombination event, should not be omitted from the analysis. The recombination from intermediate states, as well as from all of the subsequent states paving the way toward contact states, is not probable, because the lifetimes of all of these states are quite long as compared to the inverse transition rates among them. In other words, the recombination occurs almost exclusively from the initial CT state. We may therefore assume that the only rate-limiting step during charge separation is the escape from the initial strongly bound CT state x_{init}. The separation yield is then determined by the competition between the recombination rate in the initial CT state, the escape rate from the initial CT state toward intermediate states, and the back-transfer rate from intermediate states to the initial CT state. This competition may be described using a simple kinetic model whose variables are populations of the initial CT state and intermediate states (which are considered as a single state). Recombination is possible only from the initial CT state, while contact states may be reached from intermediate states. The stationarity of the initial CT state population f_{init}^{0} demands that

$$g_{\text{init}} = (\tau_{\text{init}}^{-1} + w_{\text{inter,init}})f_{\text{init}}^{0} - w_{\text{init,inter}}f_{\text{inter}}^{0} \tag{28}$$

while a similar condition for the stationary population f_{inter}^{0} of intermediate states reads as

$$(w_{\text{init,inter}} + w_{\text{contact,inter}})f_{\text{inter}}^{0} = w_{\text{inter,init}}f_{\text{init}}^{0} \tag{29}$$

In eqs 28 and 29, g_{init} is the generation rate of the initial CT state, τ_{init} is its lifetime, $w_{\text{inter,init}}$ is the total escape rate from the initial CT state x_{init} toward intermediate states x_{inter}:

$$w_{\text{inter,init}} = \sum_{x_{\text{inter}}} w_{x_{\text{inter}}x_{\text{init}}} \tag{30}$$

and $w_{\text{init,inter}}$ is the total back-transfer rate to the initial CT state from intermediate states:

$$w_{\text{init,inter}} = \sum_{x_{\text{inter}}} w_{x_{\text{init}}x_{\text{inter}}} \tag{31}$$

The total escape rate from all of the intermediate states toward contact states is

$$w_{\text{contact,inter}} = \sum_{x_{\text{inter}}} \sum_{x_{\text{f}}}{}^{'} w_{x_{\text{f}}x_{\text{inter}}} \tag{32}$$

where, for each intermediate state x_{inter}, the summation over final states x_{f} is carried out only over the states from which further transitions toward contact states are possible (it should not include the transitions back to the initial CT state). An adaptation of eq 12 to the problem at hand gives the following expression for the separation yield:

$$\varphi = \frac{w_{\text{contact,inter}}f_{\text{inter}}^{0}}{g_{\text{init}}} \tag{33}$$

Combining eqs 28, 29, and 33, we obtain the following expression for the separation yield:

$$\varphi = \frac{1}{1 + (\tau_{\text{init}}w_{\text{inter,init}})^{-1}\left(1 + \frac{w_{\text{init,inter}}}{w_{\text{contact,inter}}}\right)} \tag{34}$$

We point out that all four quantities (τ_{init}, $w_{\text{inter,init}}$, $w_{\text{init,inter}}$, and $w_{\text{contact,inter}}$) entering eq 34 are characteristic of each disorder realization; that is, eq 34 contains no free parameters. It is then remarkable that it reproduces quite well the field-dependent separation yield for each disorder realization, and consequently the disorder-averaged separation yield, which is presented by squares in Figure 3a.

The preceding discussion suggests that the barrier the initial CT exciton has to surmount to reach a contact state is determined by the energy difference $\hbar\omega_{\text{inter}} - \hbar\omega_{\text{init}}$ between the initial CT state and the intermediate CT state exhibiting strongest coupling to the initial state. In Figure 5a,b we present distributions of energies of the intermediate (Figure 5a) and the initial (Figure 5b) CT state at $F = 0$. We estimate that the average energy difference $\langle\hbar\omega_{\text{inter}} - \hbar\omega_{\text{init}}\rangle$ is around 0.07 eV, which is smaller than the average energy difference between the lowest contact state and the initial CT state. Therefore, already at $F = 0$, the average energy barrier opposing the separation from the initial CT state is ∼3 $k_{\text{B}}T$ at room temperature. For stronger F, the height of the barrier decreases, and the barrier is almost eliminated at $F \gtrsim 10^{7}$ V/m, as is presented in more detail in Figure S2a−d.

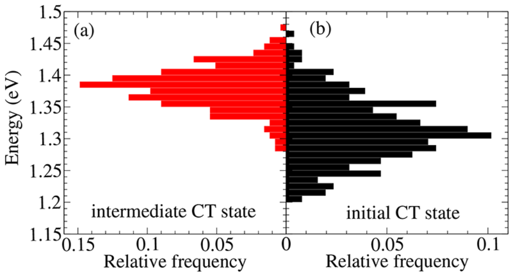

Figure 5. Histograms showing distributions of energies of (a) the intermediate CT state (which is most strongly coupled to the initial CT state) and (b) the initial CT state. The histograms are computed for $F = 0$.

Equation 34 gives the separation yield that is always an upper bound to the true separation yield obtained by numerically solving rate equations embodied in eq 10. Deriving eq 34, we assume that there is only one rate-limiting step in the process of charge separation from the initial CT state (the escape from the initial CT state to intermediate states), while further transitions from intermediate states toward contact states occur with certainty. However, in reality, some of these further transitions may present another obstacle to full charge separation, and, to fully reproduce the numerical data, eq 34 should be corrected so as to take other rate-limiting steps into account (it turns out that such corrections are really important only for strong enough disorder, vide infra). We can elaborate more on the last point by noticing that eq 34 is actually a version of the Rubel’s formula[36] that describes the separation of an exciton initially in state 1 through a series of incoherent hops $1 \rightleftharpoons 2 \rightleftharpoons \ldots \rightleftharpoons n \rightharpoonup n + 1$ among localized states, which terminates when free-charge state $n + 1$ is reached:

$$\varphi_{\text{Rubel}} = \frac{1}{1 + (\tau_1 w_{21})^{-1}\left(1 + \sum_{i=2}^{n} \prod_{j=2}^{i} \frac{w_{j-1,j}}{w_{j+1,j}}\right)} \tag{35}$$

One of the main assumptions behind the Rubel's formula is that the recombination event is possible only from the initial CT state 1, its rate being τ_1^{-1}. This assumption is satisfied in our computations, as we obtain that the major part of recombination events occurs from the initial CT state, so that we may identify τ_{init} in eq 34 with τ_1 in eq 35. The first rate-limiting step is the escape from the initial CT state to more separated (and thus longer-lived) intermediate states, which justifies the identification of $w_{\text{inter,init}}$ in eq 34 with w_{21} in eq 35. Further rate-limiting steps are taken into account in eq 35 by the term $\sum_{i=2}^{n} \prod_{j=2}^{i} \frac{w_{j-1,j}}{w_{j+1,j}}$, which takes care of the fact that, at each step j that has to be completed to reach state i, there is a competition between the escape rate $w_{j+1,j}$ toward the free-charge state n+1 and the back-transfer rate $w_{j-1,j}$ toward the initial state 1. Rubel et al. have assumed that the pathway from the initial to the final state is such that hops are possible only between neighboring states in the sequence $1 \rightleftharpoons 2 \rightleftharpoons ... \rightleftharpoons n \rightharpoonup n+1$, while in our model hops are in principle possible among any two exciton states. Thus, in our model it is difficult to isolate particular separation paths and ensure that they do not interfere among themselves. Nevertheless, as evidenced by quite good agreement between the results presented in Figure 3a, taking into account only the first rate-limiting step is a reasonable approximation to the full numerical data. This approximation is, however, plausible only for not too strong disorder. For stronger disorder, disorder-induced localization effects become more pronounced, and, on its way toward contact states, an exciton may reach a state exhibiting strong localization. Because of its strong localization, this state is poorly coupled to other states, meaning that it may act as another recombination center, or it may "reflect" excitons toward the initial state; that is, it acts as a trap state for charge separation. Neither of these two possibilities is captured by eq 34; therefore, it cannot accurately reproduce the separation yield for stronger disorder, as we discuss in the next paragraph.

We continue our discussion on the effects of disorder by investigating the separation yield for different disorder strengths σ at zero electric field. Along with the data emerging from numerically solving eq 10, in Figure 6 we present the data obtained by means of eq 34. We observe that the dependence of φ on σ is not monotonic. For very low values of σ (typically $\sigma < 20$ meV in our one-dimensional model), contact states are generally absent from the spectrum (the disorder is so weak that disorder-induced localization effects are not pronounced), and consequently the separation yield within our model is exactly equal to zero in the majority of disorder realizations. This is different from predictions of other models describing incoherent charge separation,[36,37] according to which the separation yield is different from zero for all of the values of disorder strength down to $\sigma = 0$. Therefore, the predictions of our model are not reliable for too low disorder. Bearing in mind that typical disorder strength in organic semiconductors is considered to be of the order of 100 meV,[42] the aforementioned feature of our model does not compromise its relevance. For stronger disorder (typically $\sigma > 20$ meV), contact states start to appear in the spectrum, and their number grows with increasing σ. At the same time, the average energy difference $\langle \hbar\omega_{\text{inter}} - \hbar\omega_{\text{init}} \rangle$ between the intermediate state and the initial CT state decreases (see Figure S3), and the escape rate $w_{\text{inter,init}}$ from the initial CT state to intermediate states increases (see eq 18). Because the disorder is still not too strong, further separation from intermediate states is much more probable than the "implosion" of the pair, meaning that typically $w_{\text{init,inter}}/w_{\text{contact,inter}} \ll 1$. The last statement, combined with the fact that τ_{init} essentially does not depend on σ, gives that the separation yield determined by eq 34 increases with increasing σ. However, there exists an optimal disorder strength σ_{opt} for which the separation yield attains a maximum value, so that for $\sigma > \sigma_{\text{opt}}$ an increase in the disorder strength leads to a decreased separation yield. In our numerical computations, σ_{opt} is around 60 meV, in good agreement with the results of ref 37, which also point toward the existence of the optimal disorder strength. Although for strong disorder the number of contact states is large, the pronounced disorder-induced localization starts to impede phonon-assisted transitions among exciton states. The number of trap states for charge separation (cf., previous paragraph) increases, meaning that there is more than just a single rate-limiting step during the separation of the initial electron–hole pair. This leads to an increased probability of the "implosion" of the pair into the initial CT state or the pair recombination directly from trap states. Therefore, the separation yield is decreased. As can be inferred from Figure 6, the yield computed using eq 34 (circles) is again an upper bound to the separation yield obtained by numerically solving rate equations (eq 10, squares) and approximates it quite well only for $\sigma \lesssim \sigma_{\text{opt}}$, while for $\sigma > \sigma_{\text{opt}}$ the two separation yields exhibit opposite trends with increasing disorder strength. While the true separation yield decreases for $\sigma > \sigma_{\text{opt}}$, the yield given by eq 34 monotonically increases in the entire examined range of disorder strength, consistent with the fact that $\langle \hbar\omega_{\text{inter}} - \hbar\omega_{\text{init}} \rangle$ monotonically decreases with increasing σ. Equation 34 does not capture further rate-limiting steps in the course of charge separation, and the highly successful escape from the initial CT state to intermediate states does not guarantee full charge separation.

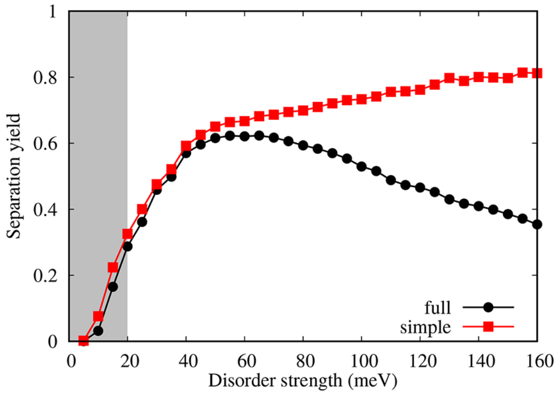

Figure 6. Yield of charge separation from the strongly bound CT state at $F = 0$ for different strengths σ of the diagonal static disorder. The gray area indicates the range of disorder strength in which the predictions of our model are not reliable. The data labeled by "full" are obtained by numerically solving rate equations (eq 10), while the data labeled by "simple" are computed using eq 34.

The apparent simplicity of our model enables us to systematically study the effects of variations of different model parameters on the efficiency of charge separation starting from the strongly bound CT state. Let us first examine how the variations in the electron delocalization in the acceptor (mimicked by variations in the transfer integral $J_{\mathrm{A},0}^{\mathrm{c,int}}$) and in the hole delocalization in the donor (mimicked by variations in the transfer integral $J_{\mathrm{D},0}^{\mathrm{v,int}}$) affect the separation yield. We obtain that better delocalization of carriers promotes higher separation yields; see Figure 7a,b. This can be rationalized using eq 34, which determines the separation yield as a function of only a couple of parameters, and following the variation of these parameters with varying carrier delocalization. When the separation yield is high (greater than 0.8 already at zero field and for the lowest investigated values of $J_{\mathrm{A},0}^{\mathrm{c,int}}$ and $J_{\mathrm{D},0}^{\mathrm{v,int}}$, cf., the discussion of Figure 4a−d), reasonable variations in $J_{\mathrm{A},0}^{\mathrm{c,int}}$ and $J_{\mathrm{D},0}^{\mathrm{v,int}}$ do not dramatically influence the separation yield, which remains high. When the separation yield is low or intermediate (less than 0.8 at zero field and for the lowest investigated values of $J_{\mathrm{A},0}^{\mathrm{c,int}}$ and $J_{\mathrm{D},0}^{\mathrm{v,int}}$), it exhibits a pronounced increase with increasing transfer integrals $J_{\mathrm{A},0}^{\mathrm{c,int}}$ and $J_{\mathrm{D},0}^{\mathrm{v,int}}$. Better carrier delocalization leads to an increase in the escape rate $w_{\mathrm{inter,init}}$ from the initial CT state, which, along with the fact that τ_{init} remains largely unaffected by variations in $J_{\mathrm{A},0}^{\mathrm{c,int}}$ and $J_{\mathrm{D},0}^{\mathrm{v,int}}$, means that the separation yield determined by eq 34 is higher.

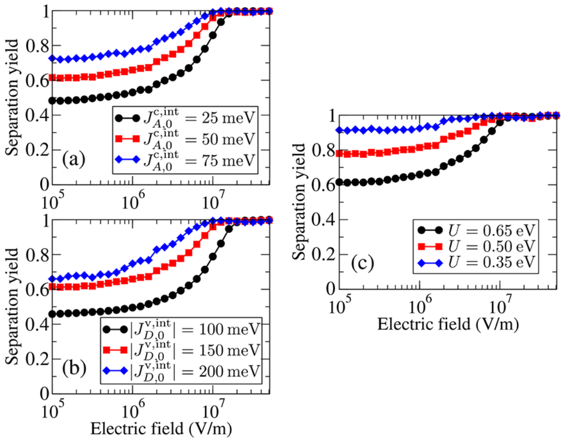

Figure 7. Field-dependent separation yield from the strongly bound CT state for different values of (a) the electron transfer integral $J_{\mathrm{A},0}^{\mathrm{c,int}}$ in the acceptor, (b) the hole transfer integral $J_{\mathrm{D},0}^{\mathrm{v,int}}$ in the donor, and (c) the on-site Coulomb interaction U.

Next, we comment on the variations that the separation yield undergoes when the magnitude of the on-site Coulomb interaction U is changed. In Figure 7c we observe that weaker electron−hole interaction leads to more efficient charge separation from the strongly bound CT state. Again, this beneficial effect of weaker Coulomb interaction may be attributed to the product $\tau_{\mathrm{init}} w_{\mathrm{inter,init}}$ being (on average) larger for weaker Coulomb interaction. On a more intuitive level, the trends in the separation yield presented in Figure 7a−c may be rationalized by following the changes in the disorder-averaged energy difference $\langle \hbar\omega_{\mathrm{inter}} - \hbar\omega_{\mathrm{init}} \rangle$ with changing the degree of carrier delocalization and the strength of the electron−hole interaction. In Figure S4a1−c3, we compare values of $\langle \hbar\omega_{\mathrm{inter}} - \hbar\omega_{\mathrm{init}} \rangle$, as well as the energy distributions of the initial and intermediate CT state, for different $J_{\mathrm{A},0}^{\mathrm{c,int}}$, $J_{\mathrm{D},0}^{\mathrm{v,int}}$, and U. We conclude that better carrier delocalization and weaker electron−hole interaction favor lower values of $\langle \hbar\omega_{\mathrm{inter}} - \hbar\omega_{\mathrm{init}} \rangle$, or, in other words, lower the separation barrier from the CT state. Let us also note that each of the effects studied can on its own improve the separation from the strongly bound CT state, because its binding energy strongly depends both on the degree of carrier delocalization and on the Coulomb interaction; compare to the discussion of the results (Figure 11a−c) concerning charge separation from the closely separated donor exciton state.

We have also studied the temperature dependence of the process of charge separation from the strongly bound CT state. We observe an approximately 6-fold decrease in the separation yield when the temperature is decreased from 300 to 100 K; see Figure 8a. On temperature reduction from 300 to below 50 K, the separation yield reduces for more than an order of magnitude. These observations are in agreement with other numerical studies of charge separation from the strongly bound CT state,[34] and with experimentally obtained temperature dependence of the photocurrent under an excitation at the low-energy edge of the CT manifold.[65]

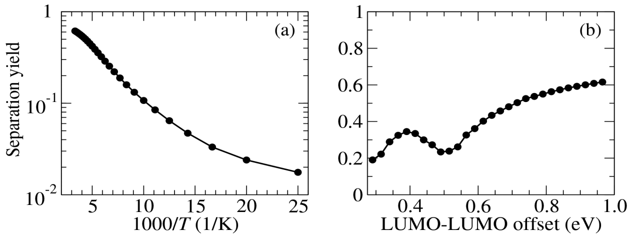

Figure 8. Yield of charge separation from the strongly bound CT state at zero electric field as a function of (a) the temperature (in Arrhenius representation) and (b) the LUMO−LUMO offset. The reported values of the LUMO−LUMO offset refer to the ordered system.

The effect of the variations in the LUMO−LUMO offset on the separation yield was studied by changing average on-site energies $\varepsilon_{\mathrm{A},0}^{\mathrm{c}}$, $\varepsilon_{\mathrm{A},1}^{\mathrm{c}}$, and $\varepsilon_{\mathrm{A},0}^{\mathrm{v}}$ in the acceptor part of the bilayer (see Figure 1) by the same amount, keeping all of the other model parameters listed in Table 1 unchanged. In first approximation, these variations manifest themselves in Figure 2a−e as rigid translations of the DOS of space-separated exciton states (Figure 2b−d) with respect to the DOS of donor and acceptor exciton states (Figure 2a,e). Figure 8b presents the dependence of the separation yield at zero electric field on the LUMO−LUMO offset. For the LUMO−LUMO offset greater than approximately 0.5 eV, we observe that the separation yield monotonically decreases with decreasing the LUMO−LUMO offset; see Figure 8b. A decrease in the LUMO−LUMO offset leads to a decreased energy difference between the lowest acceptor (and also donor) state and the initial CT state; see also Figure 2a−e. We may thus expect that a sufficient decrease in the LUMO−LUMO offset results in the involvement of acceptor and donor states in the separation from the strongly bound CT state. The transitions from the space-separated manifold toward the acceptor (donor) manifold are in general much less probable than those inside the space-separated manifold. However, once an exciton enters the acceptor (donor) manifold, it can easily recombine, because the typical lifetime of acceptor (donor) states is shorter than the lifetime of the initial CT state. In other words, the fact that acceptor (donor) states participate in the separation of the strongly bound CT exciton is seen as a decrease in the separation yield, which is due to the enhanced recombination from acceptor (donor) states. This is shown in more detail in Figure S5a,b, which provide data on recombination from different groups of exciton states. While the recombination from acceptor states can partially account for the decrease in

DOI: 10.1021/acs.jpcc.8b03114
J. Phys. Chem. C 2018, 122, 10343−10359

the separation yield observed for LUMO−LUMO offsets below 0.65 eV, the recombination from donor states is reflected in the decrease seen for LUMO−LUMO offsets below 0.4 eV. We can estimate these numbers using Figure 2a−e and having in mind that the LUMO−LUMO offset for that arrangement of exciton energies is ca. 0.97 eV. A rigid translation of Figure 2b−d by approximately 0.3 eV (upward in energy) makes the initial CT state energetically close to the acceptor states in the low-energy tail of the acceptor DOS, meaning that they can participate in the separation of the initial CT state. Similarly, a rigid translation of Figure 2b−d by approximately 0.55 eV makes the initial CT state energetically close to the donor states in the low-energy tail of the donor DOS. However, to understand the behavior of the separation yield in the whole range of LUMO−LUMO offsets displayed in Figure 8b, we have to remember that lower LUMO−LUMO offset promotes better coupling between the two parts of the bilayer, which is mediated by the D/A couplings J^c_{DA} and J^v_{DA}. As a consequence, reducing the LUMO−LUMO offset enhances the electron−hole overlap in CT states, thus decreasing their lifetime and increasing the recombination from CT states, which is shown in Figures S6 and S5b. Therefore, enhanced recombination from CT states can explain the decrease in the separation yield observed for LUMO−LUMO offsets above approximately 0.65 eV.

Charge Separation from a Donor Exciton State. Here, we aim at understanding which factors control charge separation starting from a donor exciton state. In numerical computations, the generation rate g_x appearing in eq 10 is set to a nonzero value only for donor states. We have noted in our previous publications that the low-energy (closely separated and strongly bound) donor states are essentially isolated from the manifold of space-separated states and thus act as trap states for the separation of the initial donor excitons on subpicosecond time scales.[16,17] On the contrary, higher-energy (more separated and loosely bound) donor states exhibit appreciable coupling to the space-separated manifold, and we may thus expect that charge separation starting from these states should be more probable than that starting from closely separated donor states.

We perform computations of the yield of the separation of donor excitons of different energies. We focus on the energy windows centered around E_{init} = 2.0 eV (the optical gap of the ordered donor material), E_{init} = 2.1 eV, and E_{init} = 2.2 eV (significantly above the optical gap of the ordered donor material), which is indicated by horizontal arrows in Figure 2a. Because the precise energies of donor states are determined by the disorder, we choose the initial donor state among the states that lie in the 50 meV-wide energy windows centered around the aforementioned energies. One particular donor state out of the chosen states is selected by the requirement that the squared modulus of the dipole moment for the direct generation of donor exciton state x, which is proportional to $\left|\sum_{i\in \mathrm{D};\alpha_i\beta_i} \psi^x_{(i\alpha_i)(i\beta_i)}\right|^2$,[16] be maximum. In other words, among donor states in a given energy window, we select the state whose direct generation from the ground state is most probable. Such a choice of the initial donor state is motivated by our recent computations in which we have observed that quite a high fraction of photogenerated excitons remain in the initially photoexcited donor state on a picosecond time scale following the excitation.[16]

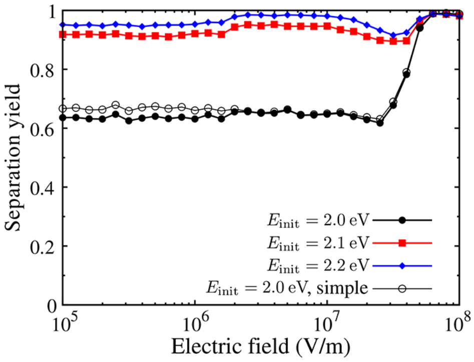

Figure 9. Field-dependent yield of charge separation starting from donor exciton states of different energies. The data represented by filled symbols are obtained by solving the full set of rate equations (eq 10). The data represented by empty circles are obtained by solving the reduced set of rate equations (eq 36) in case E_{init} = 2.0 eV.

In Figure 9, we compare the yields of charge separation starting from donor states of different energies. As we have expected, charge separation starting from a higher-energy donor state is more efficient than that starting from a closely separated donor state. The yield of the separation from a donor state situated around E_{init} = 2.2 eV is practically field-independent and greater than 0.9 for all of the examined values of the electric field down to $F = 0$. The yield is somewhat higher for E_{init} = 2.2 eV than for E_{init} = 2.1 eV. On the other hand, the yield of the separation from a closely separated donor state (E_{init} = 2.0 eV) is lower: it is almost constant for electric fields $F \lesssim 5 \times 10^7$ V/m, its value being around 0.6, after which it rises and reaches values close to 1 at $F \sim 10^8$ V/m. The value of the electric field at which the separation from a closely separated donor state occurs with certainty is almost an order of magnitude larger than in the case of charge separation from the strongly bound CT state, see Figure 3a, which is consistent with the fact that the binding energy of the donor exciton is larger than the binding energy of the CT exciton.

Let us now analyze in more detail the separation of the closely separated donor exciton (E_{init} = 2.0 eV). Our data suggest that the major part of recombination events occur from donor exciton states. This is consistent with the fact that phonon bath-assisted transitions starting from the closely separated donor exciton state couple it most strongly to other donor states, while coupling to the space-separated manifold is in principle much weaker (we note that its coupling to an acceptor state is practically negligible). The states of the space-separated manifold to which the closely separated donor state can couple are typically well spatially separated, long-lived, and exhibit good coupling to other space-separated states. In other words, despite the weak coupling, once an exciton in the closely separated donor state performs a transition to the space-separated manifold, it is highly probable that it will eventually reach a fully separated state. Instead of finding the stationary solution to the full set of rate equations (eq 10) for all exciton states (excluding contact states), we may compute the separation yield by solving the rate equations in which we explicitly consider only donor states $x \in \mathrm{XD}$ and treat exciton states x' that are not of donor character as absorbing states:

$$0 = g_x - \tau_x^{-1} f_x^0 - \sum_{x'} w_{x'x} f_x^0 + \sum_{x' \in \mathrm{XD}} w_{xx'} f_{x'}^0 \tag{36}$$

The separation yield, computed by inserting the solution to eq 36 into an expression analogous to eq 12, which reads as

$$\varphi = \frac{\sum_{x' \notin \mathrm{XD}} \sum_{x \in \mathrm{XD}} w_{x'x} f_x^0}{\sum_{x \in \mathrm{XD}} g_x} \tag{37}$$

is presented in case $E_{\mathrm{init}} = 2.0$ eV by empty circles in Figure 9. We note that the agreement between the two results (full and empty circles in Figure 9) is quite good, thus validating our simple picture of charge separation from a low-energy donor state. The same procedure can be repeated when considering the separation starting from higher-energy donor states, but the agreement between the results obtained by solving eq 36 and the full system of rate equations (eq 10) is worse. An analysis of recombination events suggests that, in these cases, the acceptor exciton states are an equally important recombination channel as the donor exciton states. When the initial donor state is loosely bound, its direct coupling to acceptor states cannot be neglected. Further discussion on the limits of validity of the simple picture of charge separation from donor states embodied in eq 36 is presented in the next paragraph.

We now turn to the influence of the diagonal static disorder on the yield of charge separation starting from donor exciton states of different energies at zero electric field. We focus our attention on the initial donor states whose energies are around $E_{\mathrm{init}} = 2.0$ eV and $E_{\mathrm{init}} = 2.2$ eV. Together with the separation yield emerging from numerically solving the full set of rate equations given in eq 10 (the true separation yield), in Figure 10a,b we also present the data obtained by solving the reduced set of rate equations (eq 36). We observe that the separation yield exhibits similar trends with varying disorder strength as when the separation starts from the strongly bound CT state (cf., Figure 6). In particular, for not too strong disorder, the yield increases with increasing disorder strength, it attains the maximum value when the disorder assumes its optimal value, after which it decreases. For all of the examined values of disorder strength, the yield of the separation starting from the donor state of energy $E_{\mathrm{init}} = 2.2$ eV is higher than in the case $E_{\mathrm{init}} = 2.0$ eV; compare data represented by circles in Figure 10a,b, which again suggests that excitons initially in higher-energy donor states separate more efficiently than those initially in lower-energy donor states. While the maximum yield of separation starting from the donor state of energy $E_{\mathrm{init}} = 2.0$ eV is around 0.7, the maximum yield in the case $E_{\mathrm{init}} = 2.2$ eV is above 0.9. For both initial states of charge separation, the yield computed by numerically solving the reduced set of rate equations (squares in Figure 10a,b) is an upper bound to the true separation yield (circles in Figure 10a,b) for all of the examined values of σ. For $E_{\mathrm{init}} = 2.0$ eV, the separation yield computed by solving the reduced set of rate equations reproduces the true separation yield very well when the disorder strength is from around 40 meV to around 90 meV, while for stronger disorder the agreement between the yields computed in two manners deteriorates. This suggests that, for moderate disorder strength, our simple picture of charge separation from the closely separated donor state, embodied in eq 36, is plausible. At stronger disorder, the localization effects become more important, and recombination may occur from states that do not belong to the donor manifold as well. On the other hand, the agreement between the two separation yields in case $E_{\mathrm{init}} = 2.2$ eV, see Figure 10b, is less satisfactory than that in case $E_{\mathrm{init}} = 2.0$ eV.

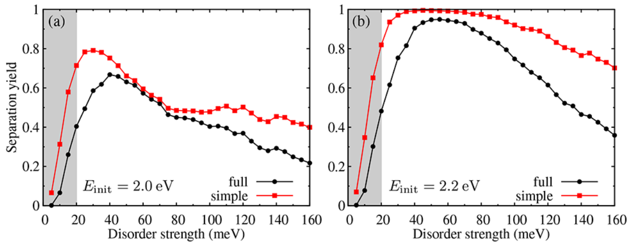

Figure 10. Separation yield at zero electric field for different strengths σ of the diagonal static disorder. The initial state of charge separation is a donor exciton state of energy around (a) $E_{\mathrm{init}} = 2.0$ eV and (b) $E_{\mathrm{init}} = 2.2$ eV. The data labeled by "full" are obtained by numerically solving the full set of rate equations (eq 10), whereas the data labeled by "simple" emerge from the numerical solution to the reduced set of rate equations (eq 36). Similar to Figure 6, the gray area indicates the range of disorder strength in which the predictions of our model are not reliable.

We have also examined the dependence of the separation yield starting from the closely separated donor state on the magnitude of electron ($J_{\mathrm{D},0}^{\mathrm{c,int}}$) and hole ($J_{\mathrm{D},0}^{\mathrm{v,int}}$) transfer integrals in the donor part of the bilayer. We find that reasonable variations in these quantities do not induce major changes in the separation yield; see Figure 11a,b. The reason for this behavior is the fact that the donor exciton binding energy, which is a rough measure of the energy barrier that has to be overcome for free charges to form, is not strongly dependent on the carrier delocalization in the donor. The factor that primarily determines the binding energy of the donor exciton is the strength of the Coulomb interaction. In Figure 11c we present the field-dependent separation yield for different values of the on-site Coulomb interaction U. As anticipated, we find that lowering U leads to a higher separation yield.

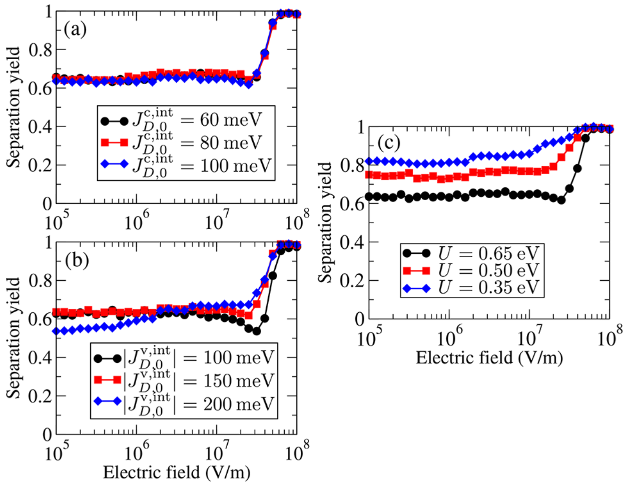

Figure 11. Field-dependent yield of charge separation starting from the closely separated donor exciton state ($E_{\mathrm{init}} = 2.0$ eV) for different values of (a) the electron transfer integral $J_{\mathrm{D},0}^{\mathrm{c,int}}$ in the donor, (b) the hole transfer integral $J_{\mathrm{D},0}^{\mathrm{v,int}}$ in the donor, and (c) the on-site Coulomb interaction U.

The temperature-dependent separation yield at zero electric field is shown in Figure 12a. We see that lower temperature leads to lower separation yield because the phonon bath-assisted processes transferring an exciton in a donor state to the space-separated manifold (and, eventually, to a state of fully separated charges) are weaker. The separation yield exhibits a 6-fold decrease when the temperature is lowered from the room temperature to around 50 K. The intensity of the temperature

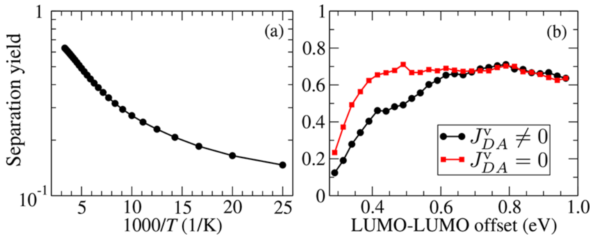

Figure 12. Yield of charge separation starting from the closely separated donor state (E_{init} = 2.0 eV) at zero electric field as a function of (a) the temperature (in Arrhenius representation) and (b) the LUMO−LUMO offset. The reported values of the LUMO−LUMO offset refer to the ordered system. In (b), we present results in which acceptor states are included ($J^{\text{v}}_{\text{DA}} \neq 0$) and excluded ($J^{\text{v}}_{\text{DA}} = 0$) from the computation.

variation-induced effect on the separation yield is somewhat smaller than in case of the separation starting from the strongly bound CT state; compare to Figure 8a.

In the end, we examine how the value of the LUMO−LUMO offset affects charge separation from the closely separated donor state. Figure 12b presents the separation yield as a function of the LUMO−LUMO offset for the values of model parameters listed in Table 1 ($J^{\text{v}}_{\text{DA}} \neq 0$, circles), as well as for $J^{\text{v}}_{\text{DA}} = 0$ (squares), that is, when states of acceptor excitons are excluded from the computation. For the LUMO−LUMO offset above approximately 0.6 eV, we observe that the separation yield in both cases is essentially the same and weakly dependent on the particular value of the LUMO−LUMO offset. This indicates that, in this range of LUMO−LUMO offsets, charge separation starting from the closely separated donor state does not involve acceptor exciton states, which once again validates our simple picture of charge separation from that state (formally embodied in eq 36). However, when the LUMO−LUMO offset is below 0.6 eV, the separation yield in case $J^{\text{v}}_{\text{DA}} \neq 0$ starts to decrease with decreasing the LUMO−LUMO offset. On the other hand, in case $J^{\text{v}}_{\text{DA}} = 0$, a similar decrease in the separation yield is observed only when the LUMO−LUMO offset is lower than approximately 0.4 eV. The different behavior of the separation yield in the two cases signalizes that, when the LUMO−LUMO offset assumes values lower than ca. 0.6 eV, states of acceptor excitons are involved in charge separation, and the observed decrease is due to the recombination from acceptor states. As we have already noted in the analysis of Figure 8b, when the LUMO−LUMO offset is around 0.6 eV, the low-energy tails of the CT and acceptor exciton DOS become energetically close. Further analysis of recombination events from different groups of exciton states, which is presented in Figure S7, shows that the contribution of the recombination from acceptor states to the total recombination probability becomes appreciable when the LUMO−LUMO offset is around 0.6 eV. When acceptor states are excluded from the computation, the independence of the separation yield on the LUMO−LUMO offset is disturbed when the energy of the strongly bound CT state is approximately equal to the energy of the initial donor state, which occurs for the LUMO−LUMO offset below around 0.4 eV. For even smaller values of the LUMO−LUMO offset, all of the space-separated states are energetically above the initial donor state, meaning that full charge separation can be achieved only by means of energetically upward processes. The decrease in the separation yield with decreasing LUMO−LUMO offset can then be attributed to an increased probability of recombination from donor states.

■ DISCUSSION

This section is devoted to a more detailed discussion of some aspects of our model.

Let us start by commenting on our results in view of the reduced dimensionality of our model. Although formally one-dimensional, the proposed model of a bilayer can be regarded as a two (or three-)-dimensional model consisting of periodically repeated chains similar to that shown in Figure 1 that are isolated from each other; that is, the transfer integrals between (neighboring) chains are equal to zero. We have established that, within our one-dimensional model, the degree of charge delocalization, quantified by the values of the electron and hole transfer integrals, is one of the factors influencing the (CT exciton) separation efficiency; see Figure 7a,b. On simple grounds, better delocalization is beneficial to charge separation because it increases the mean distance (in the direction of a single chain, which is perpendicular to the D/A interface) between the electron and hole located in the acceptor and donor, respectively. If we assigned nonzero values to transfer integrals coupling different chains, the charges could also delocalize along the direction perpendicular to the chains (parallel to the D/A interface) and further increase their separation. Therefore, it may be expected that the separation yield would be enhanced in such a genuinely two (or three-)-dimensional model. This line of reasoning is supported by studies highlighting the beneficial role of hole delocalization along polymer chains in charge separation,[28,33] particularly if we keep in mind that the values of the intrachain transfer integrals are typically larger than those employed in this study. We may also say that the separation yields we obtain using an effectively one-dimensional model are the lower limit to those that would be obtained in a higher-dimensional system. Another possible interpretation of our results is that they suggest that, to describe fundamental reasons for efficient charge separation at all-organic bilayers, it is more important to properly account for charge delocalization than for dimensionality effects.

Next, we discuss our assumptions concerning the strength of the carrier−bath interaction. We take that the polaron binding energy is E_{pol} = 15 meV, which is significantly lower than values commonly reported in electronic-structure studies of single PCBM molecules.[44,66] The selection of the values of model parameters implicitly suggests that each lattice site may be imagined to substitute a polymer chain or a group of fullerene molecules. In this regard, carrier transfer from one site to another should not be interpreted as transfer between single molecules supporting localized carrier states, but rather as transfer between two aggregates of molecules supporting delocalized carrier states. It has been demonstrated recently that, in such a case, the definition of E_{pol} (given in the text between eqs 22 and 23) should be corrected so as to take into account delocalization effects, which can substantially reduce E_{pol}.[67] Having all of these things considered, we believe that our choice of the magnitude of E_{pol} is reasonable. Larger E_{pol} (while keeping all other model parameters fixed) would result in a higher separation yield, because the phonon bath-induced transition rates (eq 18) would be larger. In this sense, our results may also be regarded as the lower limit to the separation yield computed for larger E_{pol}.

Another common choice for the spectral density $J(E)$ (eq 17) when studying charge separation in photosynthetic[55] and

DOI: 10.1021/acs.jpcc.8b03114
J. Phys. Chem. C 2018, 122, 10343−10359

OPV systems[51,68] is the so-called Drude−Lorentz spectral density. Because of its algebraic decay at high energies, the Drude−Lorentz spectral density generally favors coupling to a wider range of phonon modes than does the Ohmic spectral density employed here. In Figure S8a−d, we find that the Drude−Lorentz spectral density promotes higher separation yield than the ohmic spectral density.

The next comment concerns the number of disorder realizations over which the averaging is performed and our definition of the contact region and contact states (eqs 8 and 9). In Figure S9a,b, we present the dependence of the (average) separation yield at zero electric field on the number of disorder realizations over which we average. We see that averaging over more than 200−300 disorder realizations does not lead to substantial changes in the separation yield. Figure S10a,b confirms that our results remain qualitatively (and to a good extent quantitatively) the same when the linear dimension l_c of the contact region and the threshold probability on the right-hand sides of eqs 8 and 9 are varied within reasonable limits.

In the end, we note that an approach to the separation of strongly bound CT state similar to ours (eq 34) has been recently implemented in ref 37. We point out that eq 34 can, for moderate disorder, reproduce the separation yield in single disorder realizations without any tunable parameters. On the other hand, the authors of ref 37 reproduce the nonmonotonic dependence of the separation yield on the disorder strength using a formula similar to eq 34, which contains disorder-averaged transition rates and a tunable parameter. Let us also mention that eq 34 bears certain similarity to the exciton dissociation probability in unintentionally doped polymer materials proposed by Arkhipov et al.[69] These authors also assumed that the formation of free carriers is a two-step process: the initial exciton dissociates by the electron transfer to the dopant, while the subsequent charge separation is due to combined effects of the internal electric field, hole delocalization, and carrier recombination. However, the phenomenon of our interest, that is, the formation of free charges at D/A interfaces, is significantly different from free-charge formation in lightly doped conjugated polymers. The model introduced in ref 69 was devised to rationalize the weak field and temperature dependence exhibited by the free-charge yield in doped polymers, which is much smaller than unity. To understand very efficient charge separation at organic D/A interfaces, this model was further amended in refs 28 and 30−32.

■ CONCLUSION

Using a one-dimensional model of an all-organic bilayer, we have modeled and investigated the process of incoherent charge separation. Our model is microscopic, its parameters have clear physical significance, and their values are selected on the basis of literature data on OPV materials. The main advantage of our model is that it properly takes into account carrier delocalization, whose importance for efficient charge separation in OPV systems has been repeatedly recognized.[26−28,30,32,33] However, many studies on charge separation at organic heterointerfaces either employ the approximation of point-like charges,[34,35,61,70] or account for delocalization effects in an effective way (e.g., by introducing the carrier effective mass[26,28,30,32,33] or evenly smearing charge throughout the delocalization region[27]). On the other hand, here, carrier delocalization is fully and naturaly taken into account by working in the exciton basis. The charge separation is then conceived as a sequence of environment-assisted transitions among exciton basis states that terminates once a free-charge state is reached. Another important ingredient of our model is the diagonal static disorder, which is crucial to identify the counterparts of free-charge states within our description. We emphasize that the model and method employed in this study are very general. They may be potentially used, upon appropriate Hamiltonian modifications and suitable choice of the values of model parameters, to describe field-dependent charge generation in many different physical systems, for example, in a neat polymer materal,[14,71] or at an interface between two polymer materials.

We obtain that the synergy between moderate energetic disorder and carrier delocalization can explain quite high and relatively weakly field-dependent separation efficiencies observed in solar cells photoexcited at the low-energy edge of the CT manifold;[6] see Figure 3a. At electric fields typically encountered in a working organic solar cell ($F \sim 5-10$ V/μm), the efficiency of the separation of the strongly bound CT exciton is above 0.8. Our analytical treatment, which is sensible for not too strong disorder, reveals that the separation of the strongly bound CT exciton is actually governed by only a couple of parameters, see eq 34, among which the most important are the recombination rate from the initial CT state and the escape rate toward more separated and long-lived intermediate states. Because further separation from intermediate states can proceed without kinetic obstacles, the competition between the two aforementioned rates describes the separation quite well. However, strong disorder destroys this simple picture, because full charge separation then involves more than just a single rate-limiting step; compare the two curves in Figure 6. The remedy may then be enhancing carrier delocalization; see Figure 7a,b. This result is also in agreement with conclusions of ref 6, which emphasize that, in most efficient solar cells, the "cold" CT state is only weakly bound and quite delocalized. Moreover, we observe a much milder temperature dependence of the separation yield than the (predominantly) exponential one predicted by the Onsager−Braun model, see Figure 8a, in agreement with experimental[65] and theoretical studies.[34] The fact that larger LUMO−LUMO offsets favor more efficient free-charge generation out of the strongly bound CT state is attributed to an increased recombination probability from acceptor and donor states observed for smaller LUMO−LUMO offsets; see Figure 8b.

The separation of donor excitons is also quite efficient, and its yield depends on the exciton energy; see Figure 9. The electric field required to separate the closely separated donor exciton with certainty is almost an order of magnitude higher than that needed to separate the strongly bound CT exciton. Our results suggest that the separation of the closely separated donor exciton exhibits only one rate-limiting step, that is, the escape to the space-separated manifold. Carrier delocalization does not strongly influence this escape; see Figure 11a,b. The donor exciton separation shows weak temperature dependence, see Figure 12a, while its decrease with decreasing the LUMO−LUMO offset is attributed to the recombination from acceptor states, as in Figure 12b. Relatively weak disorder is beneficial to donor exciton separation, while strong disorder suppresses it; see Figure 10a,b.

In summary, our results provide unambiguous evidence that efficient charge separation can be achieved even out of strongly bound pair states and are supported by experiments[6,13] suggesting that free-charge generation predominantly occurs on long time scales, from localized initial conditions.

■ ASSOCIATED CONTENT

Supporting Information

The Supporting Information is available free of charge on the ACS Publications website at DOI: 10.1021/acs.jpcc.8b03114.

Numerical data complementing the discussion on the influence of various model parameters on the separation yield (PDF)

■ AUTHOR INFORMATION

Corresponding Author

*Phone: +381 (0)11 3713152. E-mail: nenad.vukmirovic@ipb.ac.rs.

ORCID

Veljko Janković: 0000-0002-0297-2167

Nenad Vukmirović: 0000-0002-4101-1713

Notes

The authors declare no competing financial interest.

■ ACKNOWLEDGMENTS

We gratefully acknowledge the support by the Ministry of Education, Science and Technological Development of the Republic of Serbia (project no. ON171017) and the European Commission under H2020 project VI-SEEM, grant no. 675121, as well as the contribution of the COST Action MP1406. Numerical computations were performed on the PARADOX supercomputing facility at the Scientific Computing Laboratory of the Institute of Physics Belgrade.

■ REFERENCES

(1) Gao, F.; Inganäs, O. Charge Generation in Polymer-Fullerene Bulk-Heterojunction Solar Cells. *Phys. Chem. Chem. Phys.* **2014**, *16*, 20291−20304.

(2) Bässler, H.; Köhler, A. "Hot or Cold": How do Charge Transfer States at the Donor-Acceptor Interface of an Organic Solar Cell Dissociate? *Phys. Chem. Chem. Phys.* **2015**, *17*, 28451−28462.

(3) Ostroverkhova, O. Organic Optoelectronic Materials: Mechanisms and Applications. *Chem. Rev.* **2016**, *116*, 13279−13412.

(4) Ponseca, C. S.; Chábera, P.; Uhlig, J.; Persson, P.; Sundström, V. Ultrafast Electron Dynamics in Solar Energy Conversion. *Chem. Rev.* **2017**, *117*, 10940−11024.

(5) Park, S. H.; Roy, A.; Beaupré, S.; Cho, S.; Coates, N.; Moon, J. S.; Moses, D.; Leclerc, M.; Lee, K.; Heeger, A. J. Bulk Heterojunction Solar Cells with Internal Quantum Efficiency Approaching 100%. *Nat. Photonics* **2009**, *3*, 297−303.

(6) Vandewal, K.; Albrecht, S.; Hoke, E. T.; Graham, K. R.; Widmer, J.; Douglas, J. D.; Schubert, M.; Mateker, W. R.; Bloking, J. T.; Burkhard, G. F.; et al. Efficient Charge Generation by Relaxed Charge-Transfer States at Organic Interfaces. *Nat. Mater.* **2014**, *13*, 63−68.

(7) Jailaubekov, A. E.; Willard, A. P.; Tritsch, J. R.; Chan, W.-L.; Sai, N.; Gearba, R.; Kaake, L. G.; Williams, K. J.; Leung, K.; Rossky, P. J.; et al. Hot Charge-Transfer Excitons Set the Time Limit for Charge Separation at Donor/Acceptor Interfaces in Organic Photovoltaics. *Nat. Mater.* **2013**, *12*, 66−73.

(8) Grancini, G.; Maiuri, M.; Fazzi, D.; Petrozza, A.; Egelhaaf, H.-J.; Brida, D.; Cerullo, G.; Lanzani, G. Hot Exciton Dissociation in Polymer Solar Cells. *Nat. Mater.* **2013**, *12*, 29−33.

(9) Bakulin, A. A.; Rao, A.; Pavelyev, V. G.; van Loosdrecht, P. H. M.; Pshenichnikov, M. S.; Niedzialek, D.; Cornil, J.; Beljonne, D.; Friend, R. H. The Role of Driving Energy and Delocalized States for Charge Separation in Organic Semiconductors. *Science* **2012**, *335*, 1340−1344.

(10) Falke, S. M.; Rozzi, C. A.; Brida, D.; Maiuri, M.; Amato, M.; Sommer, E.; de Sio, A.; Rubio, A.; Cerullo, G.; Molinari, E.; et al. Coherent Ultrafast Charge Transfer in an Organic Photovoltaic Blend. *Science* **2014**, *344*, 1001−1005.

(11) Vithanage, D. A.; Devižis, A.; Abramavičius, V.; Infahsaeng, Y.; Abramavičius, D.; MacKenzie, R. C. I.; Keivanidis, P. E.; Yartsev, A.; Hertel, D.; Nelson, J.; et al. Visualizing Charge Separation in Bulk Heterojunction Organic Solar Cells. *Nat. Commun.* **2013**, *4*, 2334.

(12) Devižis, A.; De Jonghe-Risse, J.; Hany, R.; Nüesch, F.; Jenatsch, S.; Gulbinas, V.; Moser, J.-E. Dissociation of Charge Transfer States and Carrier Separation in Bilayer Organic Solar Cells: A Time-Resolved Electroabsorption Spectroscopy Study. *J. Am. Chem. Soc.* **2015**, *137*, 8192−8198.

(13) Grupp, A.; Ehrenreich, P.; Kalb, J.; Budweg, A.; Schmidt-Mende, L.; Brida, D. Incoherent Pathways of Charge Separation in Organic and Hybrid Solar Cells. *J. Phys. Chem. Lett.* **2017**, *8*, 4858−4864.

(14) Gerhard, M.; Arndt, A. P.; Bilal, M.; Lemmer, U.; Koch, M.; Howard, I. A. Field-Induced Exciton Dissociation in PTB7-Based Organic Solar Cells. *Phys. Rev. B: Condens. Matter Mater. Phys.* **2017**, *95*, 195301.

(15) Gerhard, M.; Arndt, A. P.; Howard, I. A.; Rahimi-Iman, A.; Lemmer, U.; Koch, M. Temperature- and Energy-Dependent Separation of Charge-Transfer States in PTB7-Based Organic Solar Cells. *J. Phys. Chem. C* **2015**, *119*, 28309−28318.

(16) Janković, V.; Vukmirović, N. Identification of Ultrafast Photophysical Pathways in Photoexcited Organic Heterojunctions. *J. Phys. Chem. C* **2017**, *121*, 19602−19618.

(17) Janković, V.; Vukmirović, N. Origin of Space-Separated Charges in Photoexcited Organic Heterojunctions on Ultrafast Time Scales. *Phys. Rev. B: Condens. Matter Mater. Phys.* **2017**, *95*, 075308.

(18) Clarke, T. M.; Durrant, J. R. Charge Photogeneration in Organic Solar Cells. *Chem. Rev.* **2010**, *110*, 6736−6767.

(19) Gregg, B. A. Entropy of Charge Separation in Organic Photovoltaic Cells: The Benefit of Higher Dimensionality. *J. Phys. Chem. Lett.* **2011**, *2*, 3013−3015.

(20) Hood, S. N.; Kassal, I. Entropy and Disorder Enable Charge Separation in Organic Solar Cells. *J. Phys. Chem. Lett.* **2016**, *7*, 4495−4500.

(21) Ono, S.; Ohno, K. Combined Impact of Entropy and Carrier Delocalization on Charge Transfer Exciton Dissociation at the Donor-Acceptor Interface. *Phys. Rev. B: Condens. Matter Mater. Phys.* **2016**, *94*, 075305.

(22) Onsager, L. Initial Recombination of Ions. *Phys. Rev.* **1938**, *54*, 554−557.

(23) Braun, C. L. Electric Field Assisted Dissociation of Charge Transfer States as a Mechanism of Photocarrier Production. *J. Chem. Phys.* **1984**, *80*, 4157−4161.

(24) Wojcik, M.; Tachiya, M. Accuracies of the Empirical Theories of the Escape Probability Based on Eigen Model and Braun Model Compared with the Exact Extension of Onsager Theory. *J. Chem. Phys.* **2009**, *130*, 104107.

(25) Goliber, T. E.; Perlstein, J. H. Analysis of Photogeneration in a Doped Polymer System in Terms of a Kinetic Model for Electric-Field-Assisted Dissociation of Charge-Transfer States. *J. Chem. Phys.* **1984**, *80*, 4162−4167.

(26) Schwarz, C.; Tscheuschner, S.; Frisch, J.; Winkler, S.; Koch, N.; Bässler, H.; Köhler, A. Role of the Effective Mass and Interfacial Dipoles on Exciton Dissociation in Organic Donor-Acceptor Solar Cells. *Phys. Rev. B: Condens. Matter Mater. Phys.* **2013**, *87*, 155205.

(27) Deibel, C.; Strobel, T.; Dyakonov, V. Origin of the Efficient Polaron-Pair Dissociation in Polymer-Fullerene Blends. *Phys. Rev. Lett.* **2009**, *103*, 036402.

(28) Nenashev, A. V.; Baranovskii, S. D.; Wiemer, M.; Jansson, F.; Österbacka, R.; Dvurechenskii, A. V.; Gebhard, F. Theory of Exciton Dissociation at the Interface Between a Conjugated Polymer and an Electron Acceptor. *Phys. Rev. B: Condens. Matter Mater. Phys.* **2011**, *84*, 035210.

(29) Schwarz, C.; Bässler, H.; Bauer, I.; Koenen, J.-M.; Preis, E.; Scherf, U.; Köhler, A. Does Conjugation Help Exciton Dissociation? A Study on Poly(p-phenylene)s in Planar Heterojunctions with C_{60} or TNF. *Adv. Mater.* **2012**, *24*, 922−925.

(30) Arkhipov, V. I.; Heremans, P.; Bässler, H. Why is Exciton Dissociation So Efficient at the Interface Between a Conjugated

Polymer and an Electron Acceptor? *Appl. Phys. Lett.* **2003**, *82*, 4605–4607.

(31) Baranovskii, S. D.; Wiemer, M.; Nenashev, A. V.; Jansson, F.; Gebhard, F. Calculating the Efficiency of Exciton Dissociation at the Interface between a Conjugated Polymer and an Electron Acceptor. *J. Phys. Chem. Lett.* **2012**, *3*, 1214–1221.

(32) Tscheuschner, S.; Bässler, H.; Huber, K.; Köhler, A. A Combined Theoretical and Experimental Study of Dissociation of Charge Transfer States at the Donor-Acceptor Interface of Organic Solar Cells. *J. Phys. Chem. B* **2015**, *119*, 10359–10371.

(33) Athanasopoulos, S.; Tscheuschner, S.; Bässler, H.; Köhler, A. Efficient Charge Separation of Cold Charge-Transfer States in Organic Solar Cells Through Incoherent Hopping. *J. Phys. Chem. Lett.* **2017**, *8*, 2093–2098.

(34) van Eersel, H.; Janssen, R. A. J.; Kemerink, M. Mechanism for Efficient Photoinduced Charge Separation at Disordered Organic Heterointerfaces. *Adv. Funct. Mater.* **2012**, *22*, 2700–2708.

(35) Burke, T. M.; McGehee, M. D. How High Local Charge Carrier Mobility and an Energy Cascade in a Three-Phase Bulk Heterojunction Enable > 90% Quantum Efficiency. *Adv. Mater.* **2014**, *26*, 1923–1928.

(36) Rubel, O.; Baranovskii, S. D.; Stolz, W.; Gebhard, F. Exact Solution for Hopping Dissociation of Geminate Electron-Hole Pairs in a Disordered Chain. *Phys. Rev. Lett.* **2008**, *100*, 196602.

(37) Shi, L.; Lee, C. K.; Willard, A. P. The Enhancement of Interfacial Exciton Dissociation by Energetic Disorder Is a Nonequilibrium Effect. *ACS Cent. Sci.* **2017**, *3*, 1262–1270.

(38) Hoppe, H.; Sariciftci, N. S. Organic Solar Cells: An Overview. *J. Mater. Res.* **2004**, *19*, 1924–1945.

(39) Yuan, Y.; Reece, T. J.; Sharma, P.; Poddar, S.; Ducharme, S.; Gruverman, A.; Yang, Y.; Huang, J. Efficiency Enhancement in Organic Solar Cells with Ferroelectric Polymers. *Nat. Mater.* **2011**, *10*, 296–302.

(40) Savoie, B. M.; Rao, A.; Bakulin, A. A.; Gelinas, S.; Movaghar, B.; Friend, R. H.; Marks, T. J.; Ratner, M. A. Unequal Partnership: Asymmetric Roles of Polymeric Donor and Fullerene Acceptor in Generating Free Charge. *J. Am. Chem. Soc.* **2014**, *136*, 2876–2884.

(41) Liu, T.; Troisi, A. What Makes Fullerene Acceptors Special as Electron Acceptors in Organic Solar Cells and How to Replace Them. *Adv. Mater.* **2013**, *25*, 1038–1041.

(42) Bässler, H. Charge Transport in Disordered Organic Photoconductors a Monte Carlo Simulation Study. *Phys. Status Solidi B* **1993**, *175*, 15–56.

(43) Mladenović, M.; Vukmirović, N. Effects of Thermal Disorder on the Electronic Properties of Ordered Polymers. *Phys. Chem. Chem. Phys.* **2014**, *16*, 25950–25958.

(44) Cheung, D. L.; Troisi, A. Theoretical Study of the Organic Photovoltaic Electron Acceptor PCBM: Morphology, Electronic Structure, and Charge Localization. *J. Phys. Chem. C* **2010**, *114*, 20479–20488.

(45) Northrup, J. E. Atomic and Electronic Structure of Polymer Organic Semiconductors: P3HT, PQT, and PBTTT. *Phys. Rev. B: Condens. Matter Mater. Phys.* **2007**, *76*, 245202.

(46) Maillard, A.; Rochefort, A. Structural and Electronic Properties of Poly(3-hexylthiophene) π-stacked Crystals. *Phys. Rev. B: Condens. Matter Mater. Phys.* **2009**, *79*, 115207.

(47) Lan, Y.-K.; Huang, C.-I. A Theoretical Study of the Charge Transfer Behavior of the Highly Regioregular Poly-3-hexylthiophene in the Ordered State. *J. Phys. Chem. B* **2008**, *112*, 14857–14862.

(48) Cheung, D. L.; McMahon, D. P.; Troisi, A. Computational Study of the Structure and Charge-Transfer Parameters in Low-Molecular-Mass P3HT. *J. Phys. Chem. B* **2009**, *113*, 9393–9401.

(49) Street, R. A.; Hawks, S. A.; Khlyabich, P. P.; Li, G.; Schwartz, B. J.; Thompson, B. C.; Yang, Y. Electronic Structure and Transition Energies in Polymer-Fullerene Bulk Heterojunctions. *J. Phys. Chem. C* **2014**, *118*, 21873–21883.

(50) Bhatta, R. S.; Tsige, M. Chain Length and Torsional Dependence of Exciton Binding Energies in P3HT and PTB7 Conjugated Polymers: A First-Principles Study. *Polymer* **2014**, *55*, 2667–2672.

(51) Smith, S. L.; Chin, A. W. Phonon-Assisted Ultrafast Charge Separation in the PCBM Band Structure. *Phys. Rev. B: Condens. Matter Mater. Phys.* **2015**, *91*, 201302.

(52) Grancini, G.; Polli, D.; Fazzi, D.; Cabanillas-Gonzalez, J.; Cerullo, G.; Lanzani, G. Transient Absorption Imaging of P3HT:PCBM Photovoltaic Blend: Evidence For Interfacial Charge Transfer State. *J. Phys. Chem. Lett.* **2011**, *2*, 1099–1105.

(53) Liu, T.; Troisi, A. Absolute Rate of Charge Separation and Recombination in a Molecular Model of the P3HT/PCBM Interface. *J. Phys. Chem. C* **2011**, *115*, 2406–2415.

(54) Kanai, Y.; Grossman, J. C. Insights on Interfacial Charge Transfer Across P3HT/Fullerene Photovoltaic Heterojunction from Ab Initio Calculations. *Nano Lett.* **2007**, *7*, 1967–1972.

(55) Kell, A.; Feng, X.; Reppert, M.; Jankowiak, R. On the Shape of the Phonon Spectral Density in Photosynthetic Complexes. *J. Phys. Chem. B* **2013**, *117*, 7317–7323.

(56) Coropceanu, V.; Cornil, J.; da Silva Filho, D. A.; Olivier, Y.; Silbey, R.; Brédas, J.-L. Charge Transport in Organic Semiconductors. *Chem. Rev.* **2007**, *107*, 926–952.

(57) Meisel, K. D.; Vocks, H.; Bobbert, P. A. Polarons in Semiconducting Polymers: Study within an Extended Holstein Model. *Phys. Rev. B: Condens. Matter Mater. Phys.* **2005**, *71*, 205206.

(58) Proctor, C. M.; Kuik, M.; Nguyen, T.-Q. Charge Carrier Recombination in Organic Solar Cells. *Prog. Polym. Sci.* **2013**, *38*, 1941–1960.

(59) Dimitrov, S. D.; Schroeder, B. C.; Nielsen, C. B.; Bronstein, H.; Fei, Z.; McCulloch, I.; Heeney, M.; Durrant, J. R. Singlet Exciton Lifetimes in Conjugated Polymer Films for Organic Solar Cells. *Polymers* **2016**, *8*, 14.

(60) Kirchartz, T.; Taretto, K.; Rau, U. Efficiency Limits of Organic Bulk Heterojunction Solar Cells. *J. Phys. Chem. C* **2009**, *113*, 17958–17966.

(61) Offermans, T.; Meskers, S. C. J.; Janssen, R. A. J. Monte-Carlo Simulations of Geminate Electron-Hole Pair Dissociation in a Molecular Heterojunction: A Two-Step Dissociation Mechanism. *Chem. Phys.* **2005**, *308*, 125–133.

(62) Arndt, A. P.; Gerhard, M.; Quintilla, A.; Howard, I. A.; Koch, M.; Lemmer, U. Time-Resolved Charge-Transfer State Emission in Organic Solar Cells: Temperature and Blend Composition Dependences of Interfacial Traps. *J. Phys. Chem. C* **2015**, *119*, 13516–13523.

(63) Choi, J. H.; Son, K.-I.; Kim, T.; Kim, K.; Ohkubo, K.; Fukuzumi, S. Thienyl-Substituted Methanofullerene Derivatives for Organic Photovoltaic Cells. *J. Mater. Chem.* **2010**, *20*, 475–482.

(64) Deibel, C.; Strobel, T.; Dyakonov, V. Role of the Charge Transfer State in Organic Donor-Acceptor Solar Cells. *Adv. Mater.* **2010**, *22*, 4097–4111.

(65) Lee, J.; Vandewal, K.; Yost, S. R.; Bahlke, M. E.; Goris, L.; Baldo, M. A.; Manca, J. V.; Voorhis, T. V. Charge Transfer State Versus Hot Exciton Dissociation in Polymer-Fullerene Blended Solar Cells. *J. Am. Chem. Soc.* **2010**, *132*, 11878–11880.

(66) Idé, J.; Fazzi, D.; Casalegno, M.; Meille, S. V.; Raos, G. Electron Transport in Crystalline PCBM-Like Fullerene Derivatives: A Comparative Computational Study. *J. Mater. Chem. C* **2014**, *2*, 7313–7325.

(67) Taylor, N. B.; Kassal, I. Generalised Marcus Theory for Multi-Molecular Delocalised Charge Transfer. *Chem. Sci.* **2018**, *9*, 2942–2951.

(68) Yan, Y.; Song, L.; Shi, Q. Understanding the Free Energy Barrier and Multiple Timescale Dynamics of Charge Separation in Organic Photovoltaic Cells. *J. Chem. Phys.* **2018**, *148*, 084109.

(69) Arkhipov, V.; Emelianova, E.; Bässler, H. Dopant-Assisted Charge Carrier Photogeneration in Conjugated Polymers. *Chem. Phys. Lett.* **2003**, *372*, 886–892.

(70) Peumans, P.; Forrest, S. R. Separation of Geminate Charge-Pairs at Donor-Acceptor Interfaces in Disordered Solids. *Chem. Phys. Lett.* **2004**, *398*, 27–31.

(71) Menšík, M.; Pfleger, J.; Rybak, A.; Jung, J.; Ulański, J.; Halašová, K.; Vohlídal, J. Photogeneration of Free Charge Carriers in Tenuously Packed π Conjugated Polymer Chains. *Polym. Adv. Technol.* **2011**, *22*, 2075−2083.

Supporting information for: Combination of Charge Delocalization and Disorder Enables Efficient Charge Separation at Photoexcited Organic Bilayers

Veljko Janković and Nenad Vukmirović*

Scientific Computing Laboratory, Center for the Study of Complex Systems, Institute of Physics Belgrade, University of Belgrade, Pregrevica 118, 11080 Belgrade, Serbia

E-mail: nenad.vukmirovic@ipb.ac.rs

Phone: +381 (0)11 3713152.

1 Influence of Interfacial Electric Field on Charge Separation From the Strongly Bound CT State

Here, we show how the interfacial electric field affects relative positions of low-energy edges of the disorder-averaged DOS of CT (CT_0 band) and contact states. In Figure S1a-d, for four different magnitudes of the electric field, we compare low-energy edges of the disorder-averaged densities of CT (CT_0 band) and contact states along with relative-frequency histograms of the energy of the initial CT state and the lowest-energy contact state. The magnitudes of the electric field in Figure S1a-d match those reported in Figure 4a-d of the main body of the manuscript.

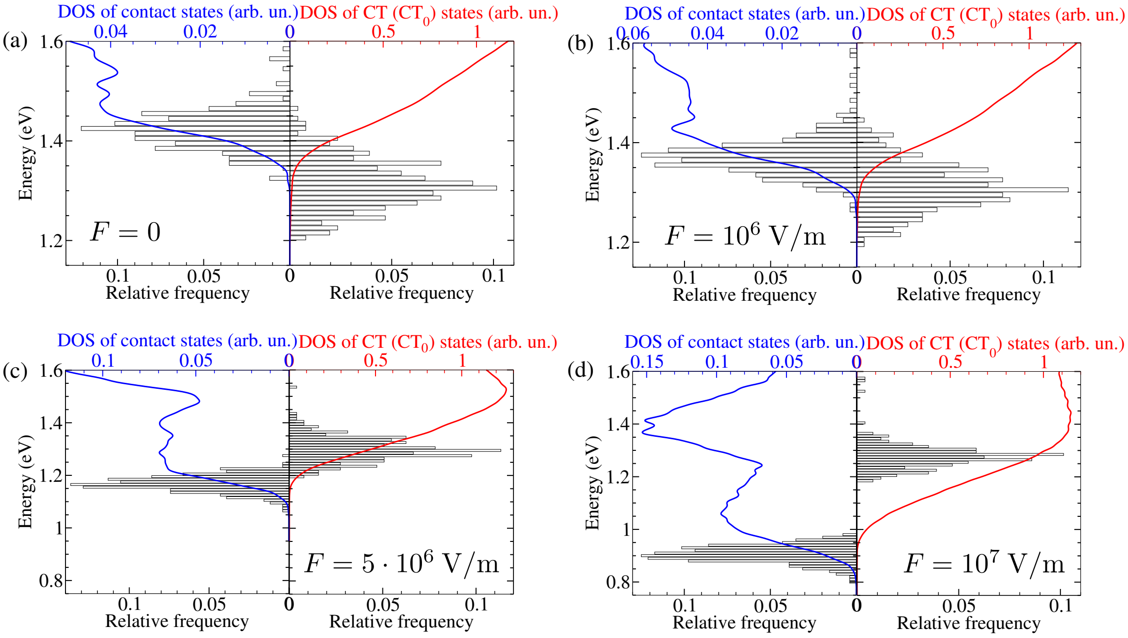

Figure S1: The low-energy tails of the DOS of CT states belonging to CT_0 band (right panel of each figure) and contact states (left panel of each figure) for different magnitudes of the interfacial electric field: (a) $F = 0$, (b) $F = 10^6$ V/m, (c) $F = 5 \cdot 10^6$ V/m, and (d) $F = 10^7$ V/m. The histograms show distributions of the energy of the initial CT state (right panel of each figure) and the lowest contact state (left panel of each figure) for different disorder realizations. The width of the bins on the energy axis is 10 meV. Note that the energy range displayed in (a) and (b) is different from the one in (c) and (d).

For relatively weak electric fields, see Figure S1a,b, the lowest-energy contact state lies energetically above the initial CT state. An increase in the interfacial electric field leads to a lower average energy difference between the initial CT state and the lowest-energy contact state, which can be estimated to be around 0.13 eV for $F = 0$ and around 0.08 eV for $F = 10^6$ V/m. However, for stronger electric fields, see Figure S1c,d, the lowest-energy contact state lies (on average) energetically below the initial CT state. We also note that increasing F moves the low-energy tails of both the DOS of CT and contact states toward lower energies, while the energy distribution of the initial CT state at the same time changes only slightly. The initial CT states lie in the tail of the CT DOS for weak F, while for stronger F the tail contains more spatially separated CT states, which is particularly pronounced in Figure S1d.

Our discussion on the separation of the strongly bound CT exciton reveals that the separation efficiency is not primarily determined by the relative position of the lowest contact state with respect to the initial CT state. Instead, the separation barrier is determined by the relative position of the initial CT state with respect to the intermediate CT state to which its coupling is strongest. For this reason, in Figure S2a-d we present the histograms of the normalized number of disorder realizations in which the initial CT state (right panel of each figure) and the intermediate CT state most strongly coupled to it (left panel of each figure) assume values in particular energy windows. The histograms are computed for the values of F matching those in Figure 4a-d of the main text and each figure is accompanied by the disorder-averaged energy difference $\langle \hbar\omega_{\text{inter}} - \hbar\omega_{\text{init}} \rangle$ between the intermediate and the initial CT state. Comparing Figure S2a-d, we observe that increasing F leads to a lower energy difference between the maxima of the two histograms, which manifests itself as lower average energy difference between the intermediate and the initial CT state. The difference between

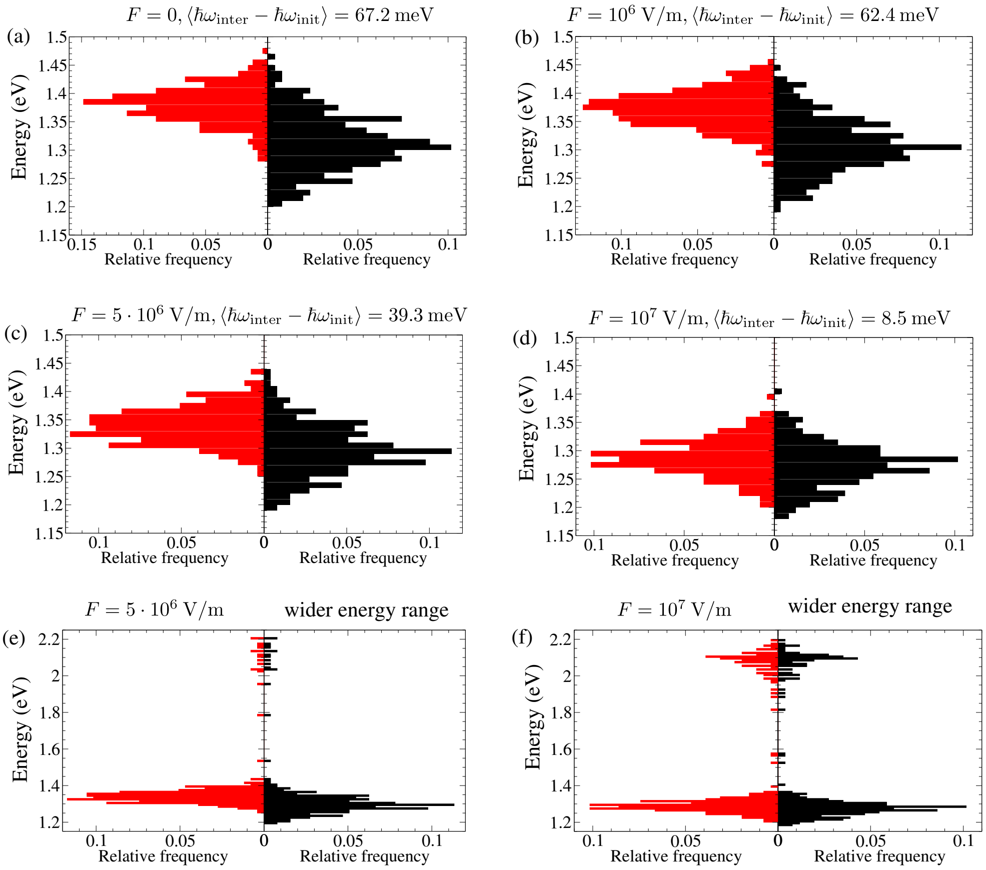

Figure S2: The histograms showing the energy distribution of the initial CT state (right panel) and the intermediate CT state (left panel) for (a) $F = 0$, (b) $F = 10^6$ V/m, (c) $F = 5 \cdot 10^6$ V/m, and (d) $F = 10^7$ V/m. In (e) and (f), we present the same histograms as in (c) and (d), respectively, but in a wider energy range.

the separation yields for $F = 0$ and $F = 10^6$ V/m is quite small, see Figure 3a of the main text, which is seen here as almost the same energy difference between the intermediate and the initial CT state. At stronger fields, the increase in the separation yield with increasing F is more pronounced, see Figure 3a of the main text, and here we observe a pronounced decrease in the energy difference $\langle \hbar\omega_{\text{inter}} - \hbar\omega_{\text{init}} \rangle$. At $F = 10^7$ V/m, the separation yield is almost equal to 1, while the energy barrier between the initial and the intermediate CT state is almost eliminated.

For the completeness of the discussion, we now focus on relatively strong interfacial electric fields, for which we have already observed (see Figure S1c,d) the displacement of the strongly bound CT state from the low-energy tail of the CT DOS toward higher energies. In Figure S2e,f we present the same histograms as in Figure S2c,d, respectively, but in a wider energy range. At stronger fields, we observe that the initial CT state chosen by our criterion (the state belonging to the CT_0 band with minimal mean electron-hole distance) may be situated in the high-energy tail of the CT DOS as well. This effect is stronger for stronger F. Still, in the majority of disorder realizations, the initial CT state is energetically close to the low-energy tail of the CT DOS.

2 Influence of Disorder on the Energy Difference between the Initial and Intermedate CT state

In Figure S3 we show the disorder-averaged energy difference $\langle \hbar\omega_{\text{inter}} - \hbar\omega_{\text{init}} \rangle$ between the intermediate and the initial CT state for different disorder strengths. We observe that $\langle \hbar\omega_{\text{inter}} - \hbar\omega_{\text{init}} \rangle$ exhibits a monotonic decrease with increasing σ.

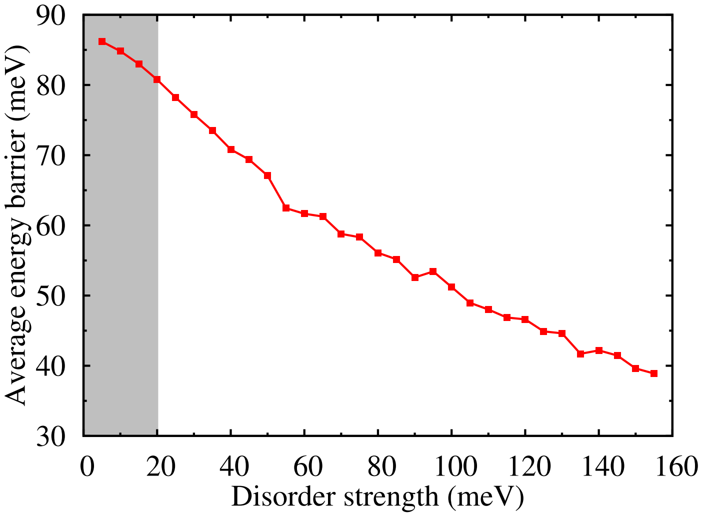

Figure S3: The disorder-averaged energy difference $\langle \hbar\omega_{\text{inter}} - \hbar\omega_{\text{init}} \rangle$ (which can also be interpreted as the average energy barrier for the separation of the initial CT exciton) as a function of the disorder strength σ. As in Figure 6 of the main text, the gray area indicates the range of disorder strength in which the predictions of our model are not reliable.

3 Further Comments on the Dependence of the Yield of the Separation from the Strongly Bound CT state on $J_{A,0}^{\mathrm{c,int}}$, $J_{D,0}^{\mathrm{v,int}}$ and U

The results to be presented here are intended to complement the discussion accompanying Figure 7a-c of the main text. Namely, in Figure S4a1-c3 we provide histograms of the energy distribution of the initial CT state (right panel of each figure) and the intermediate CT state (left panel of each figure), together with the disorder-averaged energy difference $\langle \hbar\omega_{\mathrm{inter}} - \hbar\omega_{\mathrm{init}} \rangle$ between these states. Figure S4a1-a3 is obtained for different values of $J_{A,0}^{\mathrm{c,int}}$, Figure S4b1-b3 for different values of $J_{D,0}^{\mathrm{v,int}}$, while Figure S4c1-c3 displays results for different U. In the main body of our manuscript, we emphasized that better carrier delocalization and weaker Coulomb interaction facilitate the separation of the strongly bound CT exciton. Here, we see that higher separation yields can be ascribed to smaller average energy separation between the initial and the intermediate CT state, since larger $J_{A,0}^{\mathrm{c,int}}$, larger $|J_{D,0}^{\mathrm{v,int}}|$, and smaller U lower this energy difference.

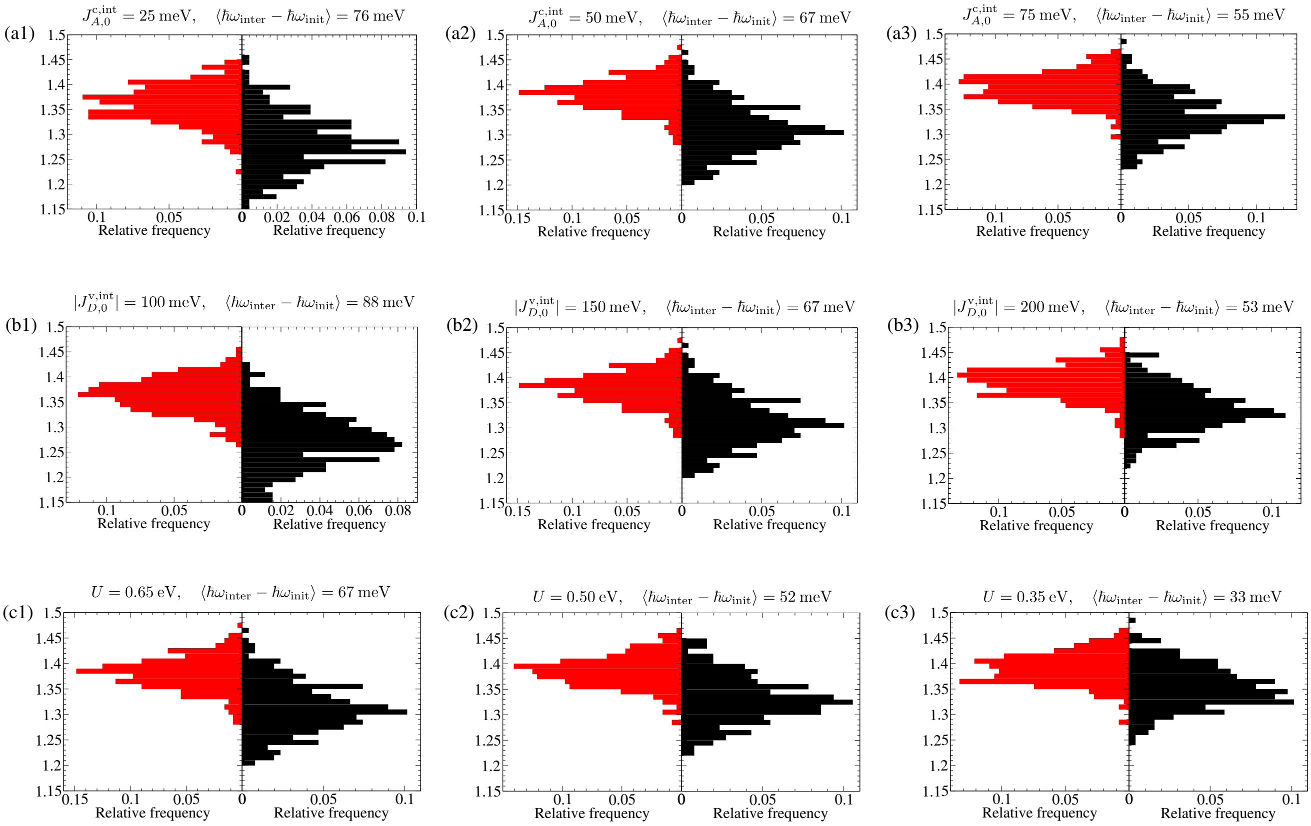

Figure S4: The histograms showing the energy distributions of the initial CT state (right panel of each figure) and the intermediate CT state (left panel of each figure) for different values of (a1-a3) electron transfer integral $J_{A,0}^{\mathrm{c,int}}$ in the acceptor, (b1-b3) hole transfer integral $J_{D,0}^{\mathrm{v,int}}$ in the donor, and (c1-c3) on-site Coulomb interaction U. Each figure is accompanied by the disorder-averaged energy difference between the initial and the intermediate CT state.

4 More Elaborate Discussion on the Dependence of the Separation from CT state on LUMO-LUMO offset

Here, we present further details on the influence of the LUMO-LUMO offset on charge separation starting from the strongly bound CT state. Along with the computation whose results are presented in the main body of our manuscript, we perform another computation of the separation yield for different LUMO-LUMO offsets in which we take $J^{\mathrm{v}}_{DA} = 0$, i.e., we exclude states of acceptor excitons from the computation. The results are presented in Figure S5a, and the comparison between them help us unveil the importance of acceptor exciton states in the separation of the strongly bound CT exciton.

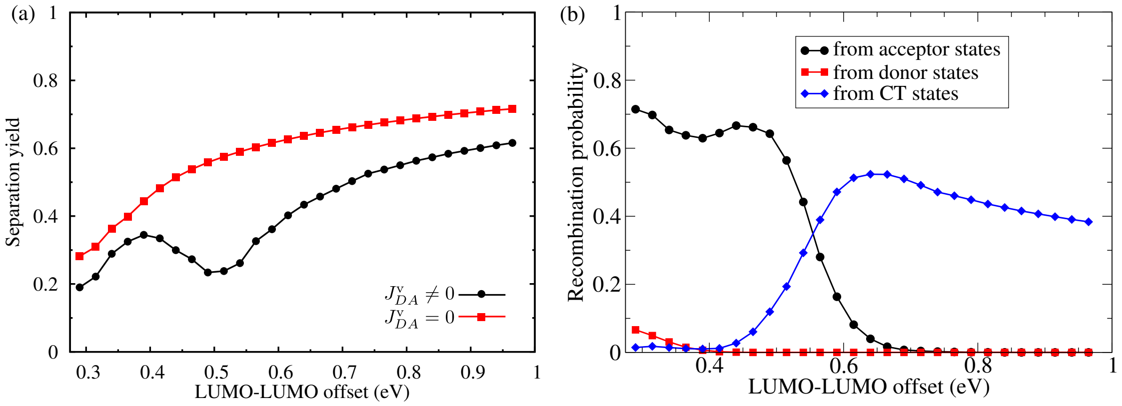

Figure S5: (a) The yield of charge separation from the strongly bound CT state at zero electric field for different LUMO-LUMO offsets and $J^{\mathrm{v}}_{DA} \neq 0$ (circles, presented also in the main text) and $J^{\mathrm{v}}_{DA} = 0$ (squares). (b) The recombination probability from acceptor (circles), donor (squares), and CT (diamonds) states for different LUMO-LUMO offsets ($J^{\mathrm{v}}_{DA} \neq 0$).

For the LUMO-LUMO offset larger than approximately 0.5 eV, the monotonic decrease in the separation yield with decreasing the LUMO-LUMO offset has two different roots. As suggested in the main text, low enough LUMO-LUMO offset (below approximately 0.65 eV) makes acceptor states participate in the separation of the strongly bound CT state. The other root, which is important for LUMO-LUMO offsets above approximately 0.65 eV, is the reduction of the lifetime of CT states that is caused by an enhanced overlap of single-particle states in the two parts of the bilayer. Namely, the lifetime of exciton state x is determined by the (weighted) spatial overlap of the electron and hole wavefunction moduli. For CT states, in which the electron and hole are located in different regions of the bilayer, this overlap is primarily determined by the values of the D/A transfer integrals J^{c}_{DA} and J^{v}_{DA}. Decreasing the LUMO-LUMO offset makes the coupling between the two parts of the bilayer more effective, meaning that the aforementioned overlap is larger and the lifetime of all the CT states is smaller, see Figure S6. Consequently, the recombination rate from CT states becomes larger, which can account for smaller separation yield with decreasing LUMO-LUMO offset.

The value of the LUMO-LUMO offset at which the involvement of acceptor exciton states becomes important may also be estimated by monitoring the amount of recombination oc-

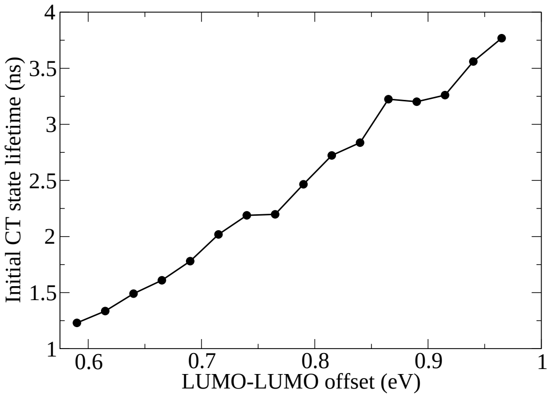

Figure S6: The disorder-averaged lifetime of the initial CT state as a function of the LUMO-LUMO offset ($J^{\mathrm{v}}_{DA} \neq 0$).

curring from acceptor states for different LUMO-LUMO offsets. In Figure S5b we depict the recombination probabilities from acceptor, donor, and CT states as functions of the LUMO-LUMO offset. While for LUMO-LUMO offsets greater than 0.6-0.65 eV the recombination predominantly occurs from CT states, for smaller LUMO-LUMO offsets recombination from acceptor states becomes nontrivial and prevails over the recombination from CT states already for LUMO-LUMO offsets smaller than ca. 0.55 eV. Therefore, in a rather wide range of LUMO-LUMO offsets (above 0.6-0.65 eV), the observed decrease in the separation yield with decreasing the LUMO-LUMO offset stems from an increase in the spatial overlap of the electron and hole in CT states. The recombination from donor states becomes important for LUMO-LUMO offsets smaller than ca. 0.4 eV (at ca. 0.4 eV, the initial CT state becomes approximately resonant with the lowest donor state), which can account for a slight decrease in the separation yield observed in this range of LUMO-LUMO offsets.

We also observe that, for all the examined values of the LUMO-LUMO offset, the separation yield for $J^{\mathrm{v}}_{DA} = 0$ is somewhat higher than for $J^{\mathrm{v}}_{DA} \neq 0$. Setting J^{v}_{DA} to 0 lowers the spatial overlap of the electron and hole in all the CT states with respect to the case $J^{\mathrm{v}}_{DA} \neq 0$, which can explain systematically larger separation yields for $J^{\mathrm{v}}_{DA} = 0$ than for $J^{\mathrm{v}}_{DA} \neq 0$.

5 Influence of the LUMO-LUMO offset on Charge Separation of the Closely Separated Donor Exciton: Analysis of Recombination Events

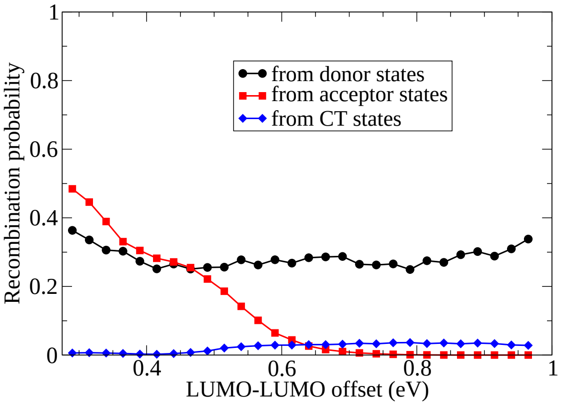

Figure S7: The recombination probability from donor (circles), acceptor (squares), and CT (diamonds) states as a function of the LUMO-LUMO offset. The separation starts from the closely separated donor exciton state ($E_{\text{init}} = 2.0\,\text{eV}$) and $J^{\text{v}}_{DA} \neq 0$.

6 Influence of the Form of Spectral Density $J(E)$ on the Separation Yield

In this section, we aim at understanding how the choice of the phonon-bath spectral density $J(E)$ we make in our manuscript affects the presented results on the yield of charge separation from CT and donor states. In the main text, we employed the Ohmic spectral density

$$J_{\mathrm{Ohm}}(E) = \eta E \mathrm{e}^{-E/E_c} \tag{1}$$

which is characterized by two parameters (η and E_c). The global measure of the strength of the interaction of carriers with the phonon bath is the polaron binding energy

$$E_{\mathrm{pol}} = \int_0^{+\infty} \mathrm{d}E \, \frac{J(E)}{E} \tag{2}$$

In other words, the contribution to E_{pol} originating from bath modes of energies between E and $E + \mathrm{d}E$ is $J(E)\,\mathrm{d}E/E$. Therefore, function

$$f(E) = \frac{J(E)}{E} \tag{3}$$

describes the contribution of bath modes of energies near E to the polaron binding energy.

Apart from the Ohmic spectral density, here we consider the so-called Drude-Lorentz spectral density

$$J_{\mathrm{DL}}(E) = \frac{2}{\pi} \, \Delta \, \frac{E \cdot \hbar\gamma}{E^2 + (\hbar\gamma)^2} \tag{4}$$

which is characterized by two parameters, Δ and $\hbar\gamma$. The polaron binding energy is $E_{\mathrm{pol,DL}} = \Delta$, while $\hbar\gamma$ determines the energy range of bath modes whose coupling to the system is appreciable. While the behavior of J_{Ohm} at large energies ($E \gg E_c$) is essentially exponential, $J_{\mathrm{DL}}(E)$ decreases only algebraically for $E \gg \hbar\gamma$. Similar situation is observed when we compare functions $f(E)$ for the two forms of spectral densities, which read as

$$f_{\mathrm{Ohm}}(E) = \mathrm{e}^{-E/E_c}, \quad f_{\mathrm{DL}}(E) = \frac{2}{\pi} \, \Delta \, \frac{\hbar\gamma}{E^2 + (\hbar\gamma)^2} \tag{5}$$

We perform computations of the separation yield using the Drude-Lorentz spectral density for which we assume that

(a) E_{pol} is the same as for the Ohmic spectral density, i.e., $\Delta = \eta E_c$;

(b) energy E^* at which the following equality holds (n is real constant), $f(E_*) = f(0)/n$, is equal to the corresponding quantity computed using the Ohmic spectral density, i.e., $\hbar\gamma = E_c \, \frac{\ln n}{\sqrt{n-1}}$.

In other words, we estimate the parameters of the Drude-Lorentz spectral density so that function $f_{\mathrm{DL}}(E)$ is in some sense similar to function $f_{\mathrm{Ohm}}(E)$. As in the main text, we take the parameters of the Ohmic spectral density $\eta = 1.5$, $E_c = 10\,\mathrm{meV}$, and we use $n = 10$ to obtain the following values of parameters of the Drude-Lorentz spectral density: $\Delta = 15\,\mathrm{meV}$ and $\hbar\gamma = 7.675\,\mathrm{meV}$. In Figure S8a,b we show $J(E)$ and $f(E)$ for the two spectral densities,

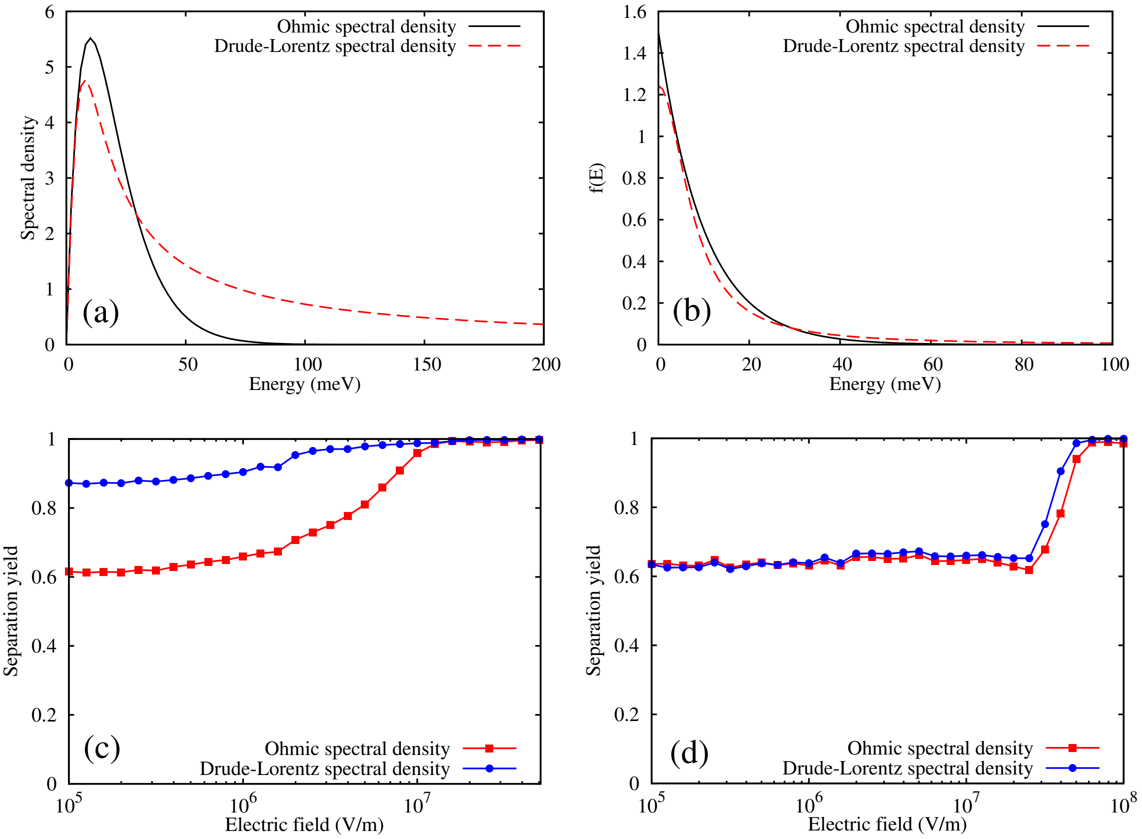

Figure S8: (a) The comparison of Ohmic (eq 1, solid line) and Drude-Lorentz (eq 4, dashed line) spectral densities. (b) The comparison of functions $f_{\mathrm{Ohm}}(E)$ and $f_{\mathrm{DL}}(E)$ (eq 5) for Ohmic (solid line) and Drude-Lorentz (dashed line) spectral density. (c) The field-dependent yield of charge separation from the strongly bound CT state for Ohmic (squares) and Drude-Lorentz (circles) spectral densities. (d) The field-dependent yield of charge separation from the closely separated donor state (energy around 2.0 eV) for Ohmic (squares) and Drude-Lorentz (circles) spectral densities.

respectively, while Figure S8c,d presents a comparison of the yield of charge separation starting from the strongly bound CT state (Figure S8c) and the closely separated donor state (Figure S8d).

We observe that the separation from the strongly bound CT state is more efficient for Drude-Lorentz than for Ohmic spectral density. This can be rationalized by comparing the two $J(E)$ curves in Figure S8a. While Ohmic spectral density favors coupling to the low-energy ($E \lesssim 50$ meV) bath modes, Drude-Lorentz spectral density also allows for appreciable coupling to the high-energy bath modes, making the number of accessible exciton states from any given exciton state larger. The number of possible intermediate CT states mediating the conversion of the initial CT exciton to free charges is therefore larger for Drude-Lorentz than for Ohmic spectral density and, consequently, the separation yield is also larger. On the other hand, the separation from the closely separated donor state does not exhibit pronounced dependence on the particular form of the spectral density. The crucial step in charge separation from the donor state is the escape out of the donor exciton manifold, which is much less probable than any of the transitions taking place within the donor manifold. The limiting factor determining the "ease" of this escape is the spatial proximity factor, which has not been changed. This is different from the separation from the CT state, where the spatial proximity factor is less important (since pairs do not leave the space-separated manifold), and the transition rate is governed by the energy-dependent factor containing $J(E)$.

7 Influence of the Number of Disorder Realization on the Separation Yield

In this section, we demonstrate that averaging over 256 disorder realizations is sufficient to provide us with reliable results. To this end, we perform a computation of the yield of charge separation from the strongly bound CT state in which we average over $32, 64, \dots, 512$ disorder realizations. In Figure S9a, we observe that, performing at least ~ 250 disorder realizations, the mean yield stabilizes around the value of 0.62 ± 0.01. Figure S9b shows that similar situation is observed in the whole investigated region of the interfacial electric fields.

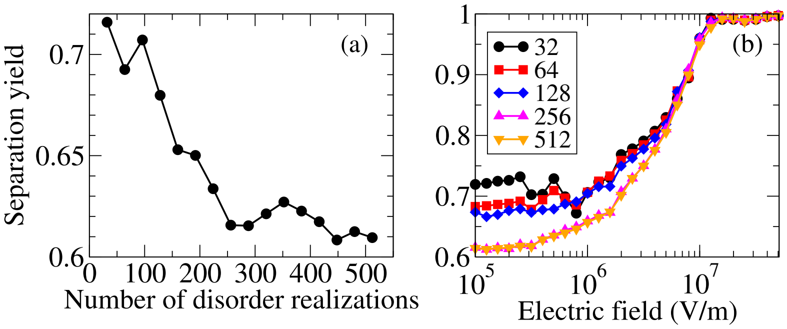

Figure S9: (a) The yield of the separation of the strongly bound CT state at $F = 0$ as a function of the number of disorder realizations over which the averaging is performed. (b) The field-dependent separation yield averaged over different number of disorder realizations.

8 Influence of the Definition of Contact States on the Separation Yield

The definition of contact states as analogues of free-charge states within our model contains two main ingredients: the dimension of the contact region l_c (in units of lattice spacing), and the minimal amount of the state localization in the contact region that permits us to identify it as a contact state. In the main body of the manuscript, we take $l_c = 11$, while the localization criteria that contact state x meets are

$$\sum_{i=0}^{l_c-1}\sum_{j}\sum_{\alpha_i\beta_j}|\psi^{x}_{(i\alpha_i)(j\beta_j)}|^2 \geq 0.7, \quad \sum_{i}\sum_{j=2N-l_c}^{2N-1}\sum_{\alpha_i\beta_j}|\psi^{x}_{(i\alpha_i)(j\beta_j)}|^2 \geq 0.7 \tag{6}$$

Here, we investigate how changes in these two quantities alter the presented results for the field-dependent separation yield from the strongly bound CT state presented. We first vary l_c, and keep the localization criteria unchanged. The changes in the field-dependent separation yield induced by these variations are summarized in Figure S10a. Then, we keep l_c unchanged, while we change the localization criteria embodied in eq 6 by changing the threshold probability of the localization of the electron and hole in the contact region, see Figure S10b. We observe that reasonable variations in both l_c and threshold probability do not induce major qualitative (and neither quantitative) changes in the results presented in the main text.

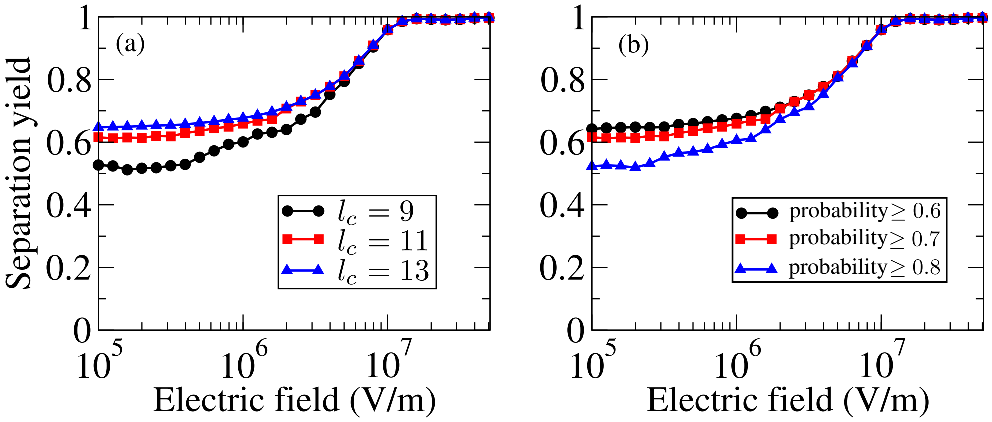

Figure S10: The field-dependent separation yield from the strongly bound CT state (a) for different lengths l_c of the contact region of the bilayer, and (b) for different threshold probabilities of the localization of the electron and hole in the contact region that permit us to identify contact states.